Experimental study on spectroscopy of laser-produced plasma for laboratory astrophysics and soft X-ray lithography application

by

Chang Liu

Submitted to the Department of Physics
in partial fulfillment of the requirements for the degree of

PhD of Science

at the

OSAKA UNIVERSITY

December 2020

Author .....
Department of Physics
Oct. 28, 2020

Certified by .....
Shinsuke Fujioka
Professor
Thesis Supervisor

Accepted by .....
Thesis committee
Department of Physics

Experimental study on spectroscopy of laser-produced plasma for laboratory astrophysics and soft X-ray lithography application

by

Chang Liu

Submitted to the Department of Physics
on Oct. 28, 2020, in partial fulfillment of the
requirements for the degree of
PhD of Science

Abstract

Spectroscopy is a widely-used diagnostic that is essentially important for understanding plasma parameters both in fundamental sciences and industrial applications. We can evaluate the temperature and density of electrons in a plasma from the width of spectral lines and line ratio, and also, we can obtain magnetic field strength in a plasma from the distance between lines separated by the Zeeman effect. This dissertation thesis consists mainly of two parts.

In the first part, I designed an experimental scheme to validate the modeling of the Zeeman effect in a high-energy-density plasma under the kilo-tesla level strong magnetic field. Zeeman splitting by kilo-tesla and mega-tesla level magnetic field were widely observed in astronomy, the next generation space X-ray observatory will also provide a possibility to observe the high-field Zeeman splitting in soft X-ray bandwidth. However, the evaluation of magnetic field from the Zeeman splitting relies heavily on numerical simulation. The motivation of this study is to investigate experimentally Zeeman effect in kilo-tesla level magnetic field for benchmarking the numerical simulation. To produce such strong magnetic field, we must use high-energy-density plasma for generating and compressing the magnetic field up to 10 kT. To generate such a strong field is a challenge for laser-plasma experiment, and to observe such a splitting a shorter bandwidth window such as extreme ultraviolet (EUV) or soft X-ray is necessary while consider about the absorption in high density plasma. The Zeeman effect is one of the measures of magnetic field strength in astronomy, however, there is no experimental data to validate the accuracy of the model and numerical code calculating the Zeeman effect in a magnetized high-energy-density plasma. I used the magneto-hydrodynamics (MHD) simulation code to optimize plasma parameters for measuring the Zeeman effect of Si ions that are plentiful in the universe. The modeling shows that we can produce 10 kT of a magnetic field in a plasma having 100 eV of electron temperature and 10^{21} cm^{-3} of electron density by compressing a low-density (5 mg/cm^3) SiO_2 foam cylinder with multiple laser beams

that are ejected from kilo-joule tera-watt laser system. I have calculated spectrum emitted from the magnetized SiO_2 plasma with consideration of the Zeeman, Stark, and Doppler effects, and the calculation reveals we can measure Si XII line at 96 eV with a soft X-ray spectrometer with achievable spectral resolution. According to the experiment design, an experiment was performed on the Gekko XII high power laser facility of Institute of Laser Engineering (ILE), Osaka university. We observed a potential sign of splitting in the experiment. Although the result is not a solid evidence for the Zeeman splitting in 10 kT field, the modeling result and experiment design still can be a guidance for the future experiments.

In the second part, I have studied the properties of hydrogen plasma photoionized with EUV light. This plasma can remove tin (Sn) contamination on the optics used in the EUV lithography system as a result of the chemical reaction $Sn+4H^* \rightarrow SnH_4$, here H^* is hydrogen radical. The optics contamination is one of the critical issues of the EUV lithography system. The optics contamination limits the operation time of the system, namely this increases the running cost of the system. We measured spectra of Balmer series emitted from photoionized hydrogen plasmas to obtain electron density, electron temperature, and hydrogen radical density of them with changing observation time and hydrogen gas pressure. Based on the experimental observation, I have proposed a mechanism of hydrogen plasma production by the EUV irradation, in which firstly EUV photons ionize hydrogen atoms, and photoionized non-thermal electrons having 100 eV of kinetic energy impact with hydrogen atoms and hydrogen ions are produced by this secondary process, and finally, the hydrogen ions recombined with thermal electrons having 1 eV of temperature and 10^{13} cm^3 of density, then rich (3.7×10^{12} cm^{-3}) hydrogen radicals are generated in a 5 Pa hydrogen gas. We have demonstrated the cleaning of the Sn contamination with the EUV-generated hydrogen radicals. The research proves the feasibility of applying the hydrogen radicals to the tin cleaning in EUV lithography.

Thesis Supervisor: Shinsuke Fujioka
Title: Professor

Acknowledgments

First of all, I would like to express the endless gratitude to my supervisor, Prof. S. Fujioka for his continuous encouragement, guidance and many discussions on researches in the past three years. He provides me the opportunity to enter another country and be a Ph.D. student in a world's famous university, Osaka University. He gave me a lot of supports not only on the research but also on personal life, and chances to participate the experiments on big science facilities in the world. But the most important thing which I have learnt from him is that if one wants to be an excellent scientist one must put 100% efforts on his work and do not wait. I will remember it in my life. I would like to thank Dr. N. Tanaka for the help and support in the last two years on the EUV-induce plasma experiment. She is not only an outstanding researcher but also a person full of humanistic concern. I can not finish the project with out her support.

The first part of this work was finished with the support from Dr. K. Matsuo Dr. A. Morace and Dr. S. Ferri for the plasma and spectrum modeling, and many illuminating discussions with Dr. B. Pollock, Dr. J Moody and Dr. HK. Chung. I also need to thank Dr. Y. Arikawa, Dr. S. Sakata, Dr. SH. Lee, Dr. Y. Abe, Dr. KFF. Law, Mr. H. Morita, Mr. J. Nishibata, Ms. M. Takemura and Mr. R. Takizawa, and all the technicians working on the Gekko-LFEX high power laser system of the Institute of Laser Engineering (ILE). I can not perform the the experiment with them. Dr. Y. Han and Ms. H. Hosokawa helps me a lot on the form target fabricating, many thanks for their efforts. I would like to thank Prof. J. Santos and Prof. R. Fedosejevs for the guidance during the LULI experiments. Their attitude on research will always encourage me.

The second part of this work is not only supported by Dr. N. Tanaka but also many support from Dr. BJ. Zhu, who was also a senior Ph.D. student and worked in a same team with me when we were in China. He is an experienced experimental researcher and suggest me a lot on the experiments, under his help the processing of this project is more efficient. Any many thanks to Prof. K. Nishihara, Prof. T.

Fujimoto and Dr. M. Goto, they provided many useful discussions and suggestion on the theoretical works. I also need to thank Samsung R&D Institute Japan (SRJ) which provides many suggestion and discussion in this research.

I would like to thank Prof. H. Azechi who is also the former director of ILE, for his kindly and detailed guidance during the first half year of my study in Japan, and thanks to the other members and former members of Laser-produced high-Field science (LF) group, Mr. Kishimoto, Mr. Ochiai, Mr. Kambayashi, Mr. SW. Guo and Mr. JY. Dun, for their daily friendliness and discussions.

I must thank to my family provides the support of my study, I can not finish my study with the help from my parents' and my aunt. Thank to Prof. JY. Zhong who is also my master's supervisor, Prof. YT. Li, Prof. FL. Wang and Prof. Z. Zhang, who gave me lots of suggestions on the future career. Specially thanks to my fiancee Ms. N. Li, she always comforts me and supports my decisions.

Finally I would thank all the old and new friends I have made in Japan: Dr. H. Li, Prof. B. Han, Dr. XY Li, Dr. QM. Pei, Prof. C. Wang, Mr. MJ. Jian, Mr. SL. Cao, Dr. YH. Zhao, Dr. W. Zhou, Ms. ZL. Yang, Ms. ZX. Niu, Mr. R. Okabe and Dr. M. Kurisu. They helped me to pass through one sleepless night after another.

Contents

List of Figures

List of Tables

Chapter 1

Introduction

Spectroscopy is an important tool of determining the physics behind the plasma related phenomena [1–4]. In this research, we will try to using the spectroscopy technology and method to detect the key plasma parameter especially the electron temperature (T_e) and number density (n_e) in both of High-Energy-Density-Physics (HEDP) plasma and EUV-induce one. Other parameters and the spectroscopy information are also included. In the first part of this research we design an experiment which intended to use the high power laser to generate a relative low density magnetized plasma, and to use the spectrometer system to observe the Zeeman splitting of spectrum [5]. The Zeeman splitting is widely observed in the nature both in the fields of atomic physics and astrophysics, but it has never been successfully observed in the high-density-laser-plasma experiment in EUV bandwidth and 10 kT level ultra strong field. For the purpose we provide some calculation of observing condition of magnetic field strength and plasma parameters, and design an experiment which may possible for the observing. In the second part we apply the spectroscopy technology to the plasma parameters and hydrogen radical measurement of EUV-induce hydrogen plasma. High intensity EUV-induce hydrogen plasma is not a well-researched area. The hydrogen Balmer lines are detected and measured, the numerical simulation results are compared with the experimental data.

Basically, the thesis is focusing on the spectroscopy technology and application of the electromagnetic wave band-width locates around ∼10 nm (∼100 eV). According to

the different academic narratives some researchers name it soft X-ray and the others ascribe it to EUV (Extreme UltraViolet). In this research, the author will not distinguishes the two conceptions in the following chapters unless necessary, considering the convenience.

Generating a strong magnetic field with laser driven capacitor-coil target makes it possible to achieve a strength of 10^2-10^3 T on the Earth [6,7]. 10^2-10^3 T is close to the surface of a compact star like a white dwarf [8–10]. Magnetic field strength is one of the most important parameters for understanding the structure of the compact stars and the strength is inferred from the Zeeman effect seen in the spectra observed with the telescope. However, the Zeeman effect has never been successfully observed in the high energy density laser plasma experiment. Laboratory experiments on the Zeeman effect will give astrophysicists valuable information to deepen the understanding of the universe. Traditional astronomical research relies heavily on observation, modeling, and numerical simulation [11–14]. High power laser can be a novel astronomical tool that makes it possible to generate magnetic fields strong enough to cause Zeeman effect in the laboratory under controlled conditions. In this research, we will focus on Zeeman spectroscopy of EUV emitted from a magnetized high energy density plasma of 10^2-10^3 T field. The goal of this project is to observe the Zeeman effect in the laboratory. This is an important physics for determining the magnetic field strength from the astronomical spectrum. Silicon is one of the abundant materials of the universe [15]. We will observe the change in the spectral shape emitted from the laser-generated magnetized silicon plasma in the EUV region with changing the magnetic field strength. Based on the laboratory measurements, there is a possibility to comparing Zeeman splitting lines in astronomical data. This potential chance may reveal how laboratory astrophysics contributes to traditional astronomical research.

The EUV light source is widely used in the semiconductor engineering applications as the technology named Extreme ultraviolet lithography (EUVL). Today EUVL utilizes laser ablation of Sn droplets as the EUV source. Since Sn contamination on the first Mo / Si mirror and following deterioration of the reflectance has been critical issue for sustainable operation of the source, many EUV sources now introduce H_2

gas to the chamber trying to clean the Sn layer. Hydrogen atom in excited electron state, so called as "hydrogen radial (H*)", is known for its chemical reaction to form stannane (SnH_4), which is gaseous states in room temperature. A H_2 molecule also interact with a photon from the EUV source resulting in hydrogen radical formation. For basic science, the EUV light source also plays an important role. The EUV produced plasma is not widely researched in the plasma physics and many atomic processing is complex and need to be determined. Recent years, researches have done some works related to EUV produced plasma. In 2016, Horst [16] used the experimental method to explore the relation between the H_2 gas pressure and the plasma electron density, and van de Ven [17] measured the ion energy distribution in EUV induced plasma. These studies give a general view of the EUV induced plasma and even give the atomic formation in it, however the plasma state is complex and highly sensitive to the external conditions. This study gives a methods to measure the accurate H* yield which can be used to determine the atomic fraction in EUV induced hydrogen plasma. It will also verify the feasibility of using EUV induced H* for industrial applications such as cleaning the Sn layers.

In the Zeeman splitting measurement, according to simulation result the Silicon plasma generate a 96 eV (12.9 nm) wavelength radiation which is selected as a potential splitting line. In the EUV-induced plasma experiment the Xe-plasma light source generate a 11 nm soft X-ray, or EUV light which is close to the Si-plasma radiation in the first project.

The thesis is organized with 6 Chapters as below:

The Chapter 1 is the introduction of this thesis.

The Chapter 2 the author introduces the laser facilities in the research, the detailed parameters is included. First section it will talk about the laser facilities, including Gekko XII and LFEX system, and the EUV experimental device. The details about the diagnostics will be introduced in the second section, including the EUV diagnostics and OES spectrometer.

The Chapter 3 the author discusses about the theoretical basis of the plasma and atomic physics which are related to this research. In the first section it will introduce

about the laser-plasma generation. Next section it will provide the principle of how to generate a strong magnetic field in the laboratory. The atomic process in a plasma and the spectrum generation will be introduced in the last section.

The Chapter 4 the author talks about the trials of detecting the Zeeman splitting in the experiment, The numerical simulation of detecting the plasma parameters will be introduced in the first section, and the next section the author will introduce the experimental design and diagnostic setting up. This part of work has been published on the journal *High Energy Density Physics* [5]. The third section the author will talks about the trials of the Zeeman splitting measurement.

The Chapter 5 the author talks about the EUV project for H* radical measurement for potential industrial application. The population of H* measurement method is introduced in the first section, and the second section the author analyzes the possible atomic process in the EUV-induced hydrogen plasma, and compares the data both from simulation and experiments. The last section the author talks about the Sn cleaning which will be a possible application of this research. This work will submit to the journal *Applied Physics letters* momentarily.

The Chapter 6 the author provides the summary of the research and the conclusion, discusses the connection of this two researches and provide the inspiration of this thesis.

Chapter 2

Laser facilities and diagnositcs

In this chapter, the author provides the facilities which are used in the thesis including the two projects. The detailed parameter of the laser facilities will be introduced in the first section. it includes the Gekko XII and LFEX systems, and the facility of the EUV experimental device. In the second section, the specification of the diagnostics will be introduced. Including the EUV spectrometer and the OES (Optical Emission Spectroscopy) system. The optical elements in the OES system are also listed so that it is possible to re-build and test by any other researchers.

2.1 Laser and EUV generation facilities

This section introduces the fore-end of the experiment facilities. The Gekko-LFEX system used in the magnetized plasma generation is briefly introduced first, and then we show the EUV-induce plasma device which is used in the second project.

2.1.1 Gekko XII and LEFX system

The Gekko XII laser was constructed in the year 1983 and it has became one of the world's few large-scale laser facilities when it was completed. The Gekko XII laser has 12 synchronized laser beams with wavelengths of 1.053 μm, peak output energy of 24 kJ and 1 ns time-duration. To date, it has been instrumental in laser fusion

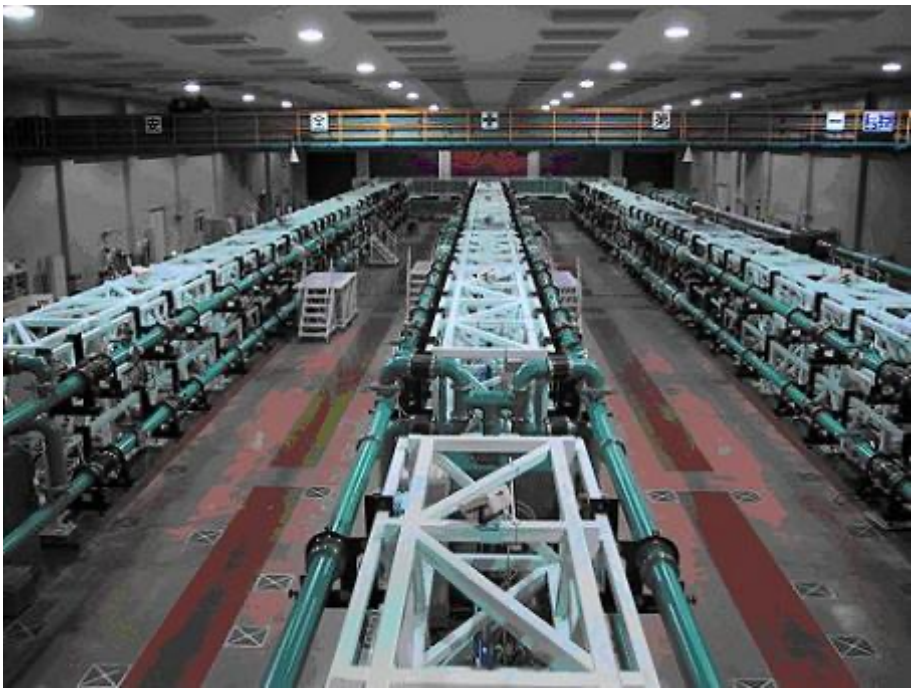

Figure 2-1: The Gekko XII system. There are 12 beams in Gekko XII facility, with 1053-527 nm in Chamber I. Pulse duration ranges 0.1 ns - 4 ns. Usually 3 or 4 shots are possible for 12 beams experiment.

research and high-energy-density physics research. The Gekko XII has driven several achievements in the areas, such as the generation of plasma with temperatures greater than one hundred million degrees Celsius, and the compression of matter to a density greater than 600 times its solid density by laser implosion [18].

The Gekko XII laser has two plasma generation vacuum chambers for conducting experimental studies. In Chamber I, a target can be irradiated by twelve laser beams arranged with spherical symmetry. The Chamber I is mainly for inertial confinement fusion (ICF) experiments. In Chamber II, a target can be irradiated by high power laser beams from a single direction by combining the twelve individual beams into a single one. This design allows higher on-target intensity for a wide range of experiments, which are from ICF experiments to laboratory astrophysics experiments. The Zeeman splitting experiment is performed on Chamber I.

The LFEX laser system provide 4 synchronized laser beam with wavelength of $1.05\mu m$ with a specification maximum output energy of 10 kJ and pulse duration from 1 to 10 ps. Seed pulse is generated by a femtosecond fiber oscillator with a

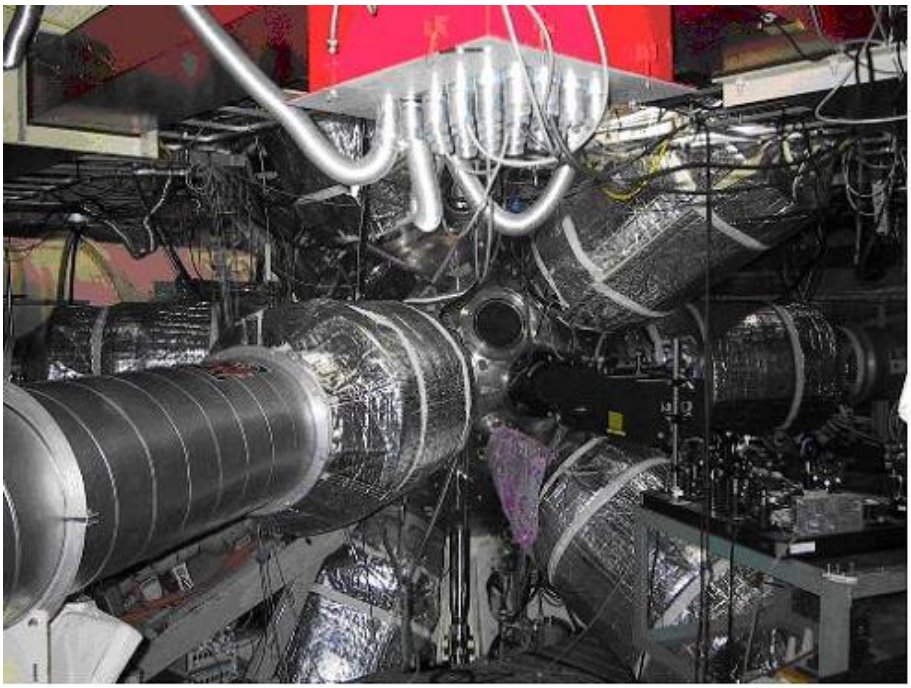

Figure 2-2: Chamber I. Beams are induced into the chamber form different direction to adapt multiple experiments.

pulse duration of 90 fs, a frequency of 100 MHz. The LFEX seed pulse is amplified by 3 Optical Parametric Chirped-pulse Amplification (OPCPA) in series, to a 6 Hz chirped-pulse output with 40 mJ, 6 nm spectral width. The chirped pulse is then amplified with two 50 mm diameter glass rod amplifier in four passes. The laser beam is then split into 4 beams, with each beam separately amplified by two rod amplifiers. Finally, the laser beam is amplified by a 2×2 array, four pass main amplifier, with 8 disk amplifiers in series on each beam [19].

By the output energy restriction, the LFEX maximum energy is limited to 500 J per beam, giving a total maximum output energy of 2 kJ in 1ps. As the spot diameter on target is about 70 μm, the LFEX intensity is about 1.6×10^{19} W cm^{-2} when the output energy at the maximum value of 2 kJ.

One of the most important mission of the LFEX laser is working as a heating laser for the ICF, but as the same time such an intensive beam is capable of MeV proton beam generation by the target normal sheath acceleration (TNSA) mechanism as well. The LFEX laser is available in the Chamber I of Gekko XII laser system and

is available to have joint shots with Gekko XII. Between two LFEX shots, the laser system need 2 hours for cooling down.

2.1.2 EUV experimental device

For the purpose of measuring the plasma parameters and H* yield, an Optical Emission Spectroscopy (OES) system was used to measure them in the H_2 / EUV interaction [20, 21]. A laser produced Xenon plasma EUV source at Institute of Laser Engineering was used in the experiment. The OES systems consist of a set of optical system, a spectrometer and control systems which are shown in the Fig. 2-3. H_α (656.3 nm), H_β (486.1 nm) and H_δ line emissions from the electron transitions of n = 3 to n = 2, n = 4 to n = 2 and n = 5 to n = 2 respectively were detected showing the existence of the H* [22]. A Nd:YAG laser (1064 nm) is induced into the vacuum chamber, radiates on a liquid-nitrogen-cooling Xenon frost target and the plasma generates which works as the EUV light source. Two elliptical total reflection mirrors reflect and focus the EUV light with 100μm radius spot size, a broad band EUV which the peak wavelength of 12 nm (103.5 eV) and intensity of 10^9 W/cm^2 to the gas cell center (GCC), with an angle about 15 degree to the central axis of gas cell [23]. The hydrogen gas is pumped in and out of the gas cell at the same time with individual pipes. There are several windows around the gas cell which are used for conducting the emission from the plasma to the diagnostics systems. The hydrogen gas pressure is controlled outside which makes a dynamic equilibrium in the gas cell, and keep the vacuum chamber with a high vacuum state (10^{-3} Pa) at the same time, or as known as "differential pumping". The EUV generator is shown in the Fig. 2-4. When the EUV radiation interact with hydrogen gas at the GCC, an EUV induced hydrogen plasma is generated. A series of experiments have been done to examine and verify the plasma states, which indicate a relative low temperature and density plasma exists.

The EUV produced plasma radiation is exported by a series lenses and mirrors. The light pass through the gas cell window, then it is reflected by the mirror 1 and converted to parallel light by the lens 1 which is shown in Fig. 2-3. The parallel light

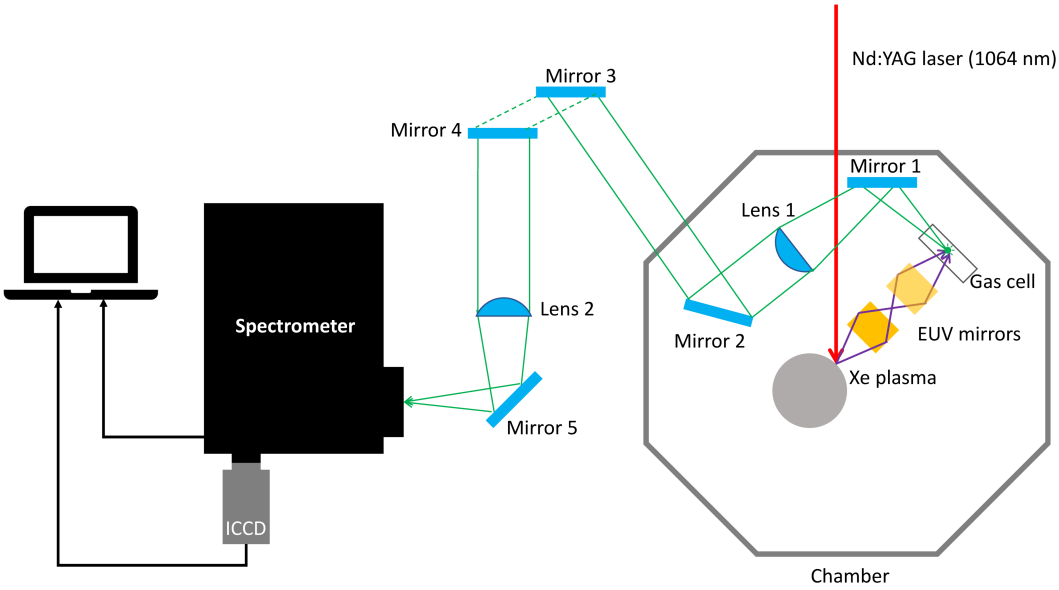

Figure 2-3: The OES system and the experimental setup. A liquid-N_2 cooling Xeon frost target are used as the EUV source, which is excited by a Nd:YAG laser (1064 nm). The EUV radiation is focused by 2 Au-coated reflect mirrors and irradiates in the focus point. The plasma emission are conducted and collect by the OES system which is consisted by optics, spectrometer and ICCD.

Table 2.1: Optics used in the OES system

Name	Description	Parameters	Produced by
Mirror 1	Al coating, 2 inch	N/A	SIGMAKOKI
Lens 1	ARC coating (400-700 nm), 2 inch	f=300mm	Thorlab
Mirror 2	Al coating, 2 inch	N/A	SIGMAKOKI
Mirror 3	Al coating, 2 inch	N/A	SIGMAKOKI
Mirror 4	Al coating, 2 inch	N/A	SIGMAKOKI
Lens 2	ARC coating (400-700 nm), 2 inch	f=300mm	Thorlab
Mirror 5	Al coating, 2 inch	N/A	SIGMAKOKI
Spectrometer	SP2500i	150/1200/2400l/mm gratings	Princeton Instruments
ICCD	PI-MAX4	1024f	Princeton Instruments

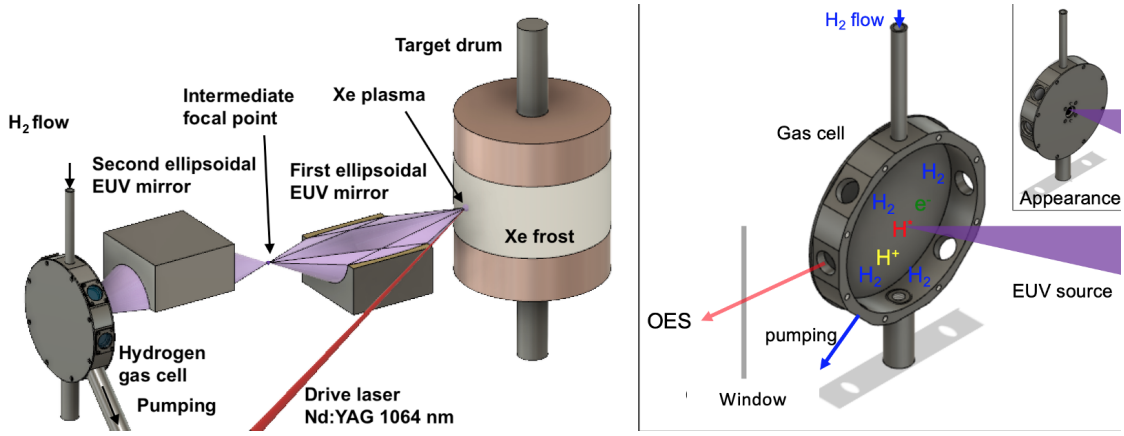

Figure 2-4: The laser-produce EUV source. The Xeon are frosted on the target drum. The Nd:YAG laser irradiates and EUV radiation is generated. The radiation is collect and focused by 2 Au-coated reflect mirrors then conducted into the gas cell. The purpose of setting up an intermediate focal point by 2 mirrors is to reduce the detritus from the drum.

will be focused again by the lens 2. The lens 1 and lens 2 are the same type which are produced by Thorlab with Anti-Reflection (AR) coated for 400-700 nm range and 300 mm focus length. As it is shown in Fig. 2-3, the light is focused on the slit of a Princeton Instruments SP2500i visible spectrometer [24]. The slit width is adjusted to 15μm. A PI-MAX4 Intensified Charged Coupled Device (ICCD) camera is coupled to the spectrometer to obtain the signal from the EUV induced hydrogen plasma [25]. Both of the ICCD and the spectrometer are controlled by a computer system with Lightfield software [26]. The detailed diagnostic parameter will be introduced in the next section.

2.2 Plasma diagnositcs

The main topic of this thesis is soft X-ray, or EUV diagnostic and application. The diagnostic system is an important part for this project. In this section, we will introduce the main diagnostic systems in the laboratory astrophysics experiment and the EUV-induce hydrogen plasma experiment. In the laboratory astrophysics experiment, which is focusing on the Zeeman splitting measurement in this project, the prior diagnostic is the EUV spectrometer. In the EUV induced hydrogen plasma

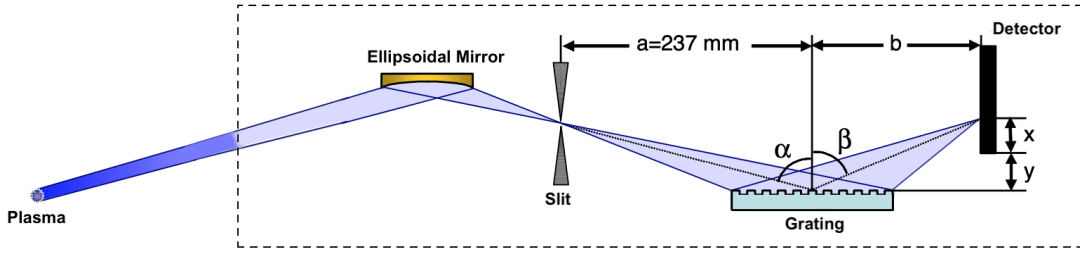

Figure 2-5: The structure of GIS. The emission from the plasma are collected by the ellipsoidal mirror in the front of the spectrometer, Then focuses on the slit.

experiment, the main diagnostic is the OES system.

2.2.1 EUV spectrometor

The EUV emitted from plasma have spectral information, and in order to measure the EUV radiation, it is necessary to disperse the light along the wave-band. In this experiment, a Grazing Incidence diffraction Spectrometer (GIS) is used. The EUV spectrum are measured using a back-illuminated Charged Coupled Device (CCD) camera as the detector. Figure 2-5 shows the configuration of the oblique-incidence type diffraction spectrometer in the EUV reflection plane [27].

The EUV emission from the plasma light source is focused on the slit by using a gold-coating ellipsoidal mirror, and the slit is used as the focus spot of the mirror to induce the light into a reflection-type diffraction grating to disperse the light. The following points need to be noticed: Firstly, the typical light amount from the plasma which is needed to be dispersed by the diffraction grating is extremely small. For this reason, an ellipsoidal mirror focus is set at the center of the slit and re-focus again at the detecting surface after the grating reflecting. It enables measurement with a high Signal to Noise (S/N) ratio. Secondly, when the diffraction grating is placed near to the plasma, on the other word which is close to the light source, The light amount will be increasing with the solid angle. Therefore, S/N ratio will be better and the detecting will become easier, but if it gets too close to the plasma, it may be contaminated by the debris. At the same time, the slit may also be contaminated, and the grazing-incidence reflecting mirror may also be deteriorated.

As the opticals such as diffraction grating is very expensive it must be used very carefully. Thirdly, since short-wavelength light such as hard X-rays is not reflected by the grazing-incidence mirror, it is possible to prevent light in these regions from entering the diffraction grating. It makes sure that the dispersed light will not be mixed with other wavelengths radiation from the light source. For the measurement waveband which has a shorter wavelength it is more effective. Lastly, using a slit as a virtual light source limits the size of plasma which we are observing, especially for the Zeeman splitting measurement which the target spectra is coming from a small region. As mentioned above, the grazing incidence spectroscope has many advantages [28]. The relationship between incident light and diffracted light can be expressed by the following Eq.2.1.

$$d(sin\alpha - sin\beta) = m\lambda \tag{2.1}$$

where d is the grating width, α and β are the angles of the two sides of the Grating normal which is shown in Fig.$2-5$, m is the mass of the particle and λ is the wavelength.

2.2.2 OES system

The OES system consisted with three main parts: Opticals (including lens and mirrors which are used to conduct the radiation of the plasma out of the gas cell), A Princeton Instruments vis-spectrometer (SP-2500 series model) and A Princeton Instruments PI-MAX4 ICCD camera. The detailed information is in Tab.2.1

According to the time resolved experiment data, the timing of 25 ns (0-50 ns for exposing) and 40 ns (20-60 ns for exposing) are used to measure the H* yield. The pressure in the gas cell is set to be 5 Pa. The Fig. 2-6 shows the entire processing of the spectra measurement. When the EUV induced plasma generates in the gas cell the light is collected by lens and then enter the OES system. The solid angle (Ω) of the system is decided by lens 1 which gives $\Omega = 0.02sr$. The light path is transferred by the optics which are consisted by 2 lenses and 5 mirrors, is already detailed shown in Fig. 2-3. The energy efficiency of the optics and spectrometer / ICCD are measured

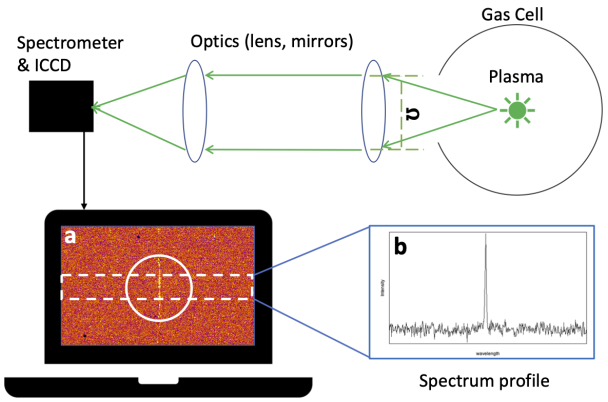

Figure 2-6: The measurement of EUV induced hydrogen plasma. The spectrum or images are observed on the screen with count, by carefully measure the system quantum efficiency (including the spectrometer / ICCD and the optics), and examine the diagnostic solid angle, it is possible to get the photon number information from the plasma.

with HeNe laser (633nm for H_α) and Cyan laser (487nm for H_β). For H_α it has an total efficiency of 3% and H_β is 4.1%. With the experimental setup which has been described in Sec. II, the spectra of H_α is shown in Fig. 2-6a. The white dashed rectangle is the selected region that plot the spectra profile (Fig. 2-6b). As the light from the plasma is refocused by lens 2 and path through the spectrometer slit, the H_α signal in the view of Fig. 2-6a is only the photons access the slit. However, the total number of photons which focused on the spectrometer slit can be calculated. In Fig. 2-6a, the H_α signal width is equal to the slit's one (15μm) and length can be regarded as the diameter (2.4 mm) of light spot (White solid cycle) which is focused by lens 2. Due to the existence of H_α and H_β line in the experiment, the two lines are used to calculate the radiation ability of the EUV induced hydrogen plasma.

Chapter 3

Plasma physics and atomic physics basics

In this chapter, we will introduce the physical process and mechanism in this research. In the first section we will talk about the basis of laser-target interaction and plasma generation. In the second section, the main topic is the strong magnetic field generation in the laboratory, and how the magnetic field affect on the spectrum. The last section will introduce about the measurement of spectrum, and what kind of information we can get from them.

3.1 Laser-plasma generation

At the irradiance of interest for the typical high-power laser facilities, which are typically 10^{12} to 10^{16} W/cm^2, the laser light immediately produces a plasma at the surface of the target. At the even higher irradiance in this range, the the laser electric field is sufficient enough to directly ionize the atoms. At the lower irradiance, the process is more complicated but nonetheless a plasma is quickly produced [29, 30]. There are three fundamental processes that occur when laser light penetrates a plasma: refraction, reflection and absorption. As the electric field of the laser pulse penetrates into a solid, part of the incident energy is absorbed, changing the state of the solid and its properties quickly. The problem of laser-matter interaction, which means the effect of

the laser electric field on matter and the inverse effect of matter on the electric field are considered simultaneously. The field equations coupled to the material equations describe the medium response to the action of the electric field. The matter considered stands for the ensemble of non-relativistic particles, electrons and nuclei that compose the solid, liquid, gas or plasma, depending on the parameters of the laser beam, namely, the intensity, wavelength, and pulse duration. Therefore, the coupled time-dependent field and material equations describe all continuous transformations of the materials [31].

Several definitions are needed to make the field of high power laser-matter interaction and its boundaries clear. First, the laser pulse is considered as of ultra-short duration if it is shorter than the duration of major relaxation processes, including the electron-to-lattice energy transfer, heat diffusion and hydrodynamics. Therefore, an atomic motion is negligible in the laser-affected solid during the pulse and the atomic structure remains intact. The associated absorbed energy density per unit volume delivered to a target allows one to study the excited solid state from subtle excitations to phase transformations, such as transition from one crystalline structure to another, from a solid to liquid, conversion to plasma, ablation, and, if the laser is focused in the bulk of a transparent dielectricâĂŤcreation of extreme pressure and temperature conditions confined inside a solid.

Second, the salient feature of the ultra-short pulse laser-matter interaction is that ultra-short pulses excite only electrons, leaving the lattice cold for the time required for the transfer of the absorbed energy from the hot electrons to the lattice. Therefore, any phase transformations in a laser-affected solid occur in non-equilibrium conditions, creating properties of the material drastically different from their equilibrium counterparts. The statistical distributions in the electron and lattice sub-systems are time-dependent, and the time required for attaining the state of equilibrium state depends heavily on the parameters of the laser pulse and the characteristics of the material.

Another important feature of the high power laser-matter interaction is that the affected area is of only a few hundred atomic layers, which relaxes within picoseconds

after the excitation. Thus, the space constraints and surface phenomena (surface states and quasi-equilibrium distribution in the outermost surface layers) are essential for understanding the phase transitions induced, such as laser ablation. Understanding the phenomena occurring on a time-scale of picoseconds and on a space-scale of nanometers is essential for high power laser-matter interaction, bringing these studies closer to research into nano-structures.

Comparing the mobility of electrons by comparison with ions, the electrons dominate for example the direct interactions of the laser with the plasma. This might lead one to expect that the thermal electrons would play a dominant role in transporting energy throughout all plasma systems. This, however, is not the case in the systems of interest here. Laboratory systems in the high-energy-density regime are typically so collisional that the electrons cannot manage to escape the ions and do not manage to affect the dynamics very strongly. It is also remarkable that there are very few astrophysical systems in which the electrons carry significant heat. The electrons, because of their small mass, are very tightly bound to the magnetic field, and the magnetic field is typically tangled enough to keep them from accomplishing any large-scale heat transport. Systems involving instabilities in loops of magnetic field, which occur for example near the Sun, or involving magnetic reconnection, which occurs in many places, produce bursts of energetic electrons. These electrons in turn radiate, so that the electron radiation can be an important diagnostic of the phenomena. However, the electrons do not dominate the overall dynamics of reconnecting systems. Likewise, the radiation from electrons has become an important indicator of cosmic-ray acceleration in supernova remnants, but the cosmic rays that actually reach the Earth are almost all ions. So electrons are important. However, with two crucial exceptions, they rarely carry much heat anywhere that matters.

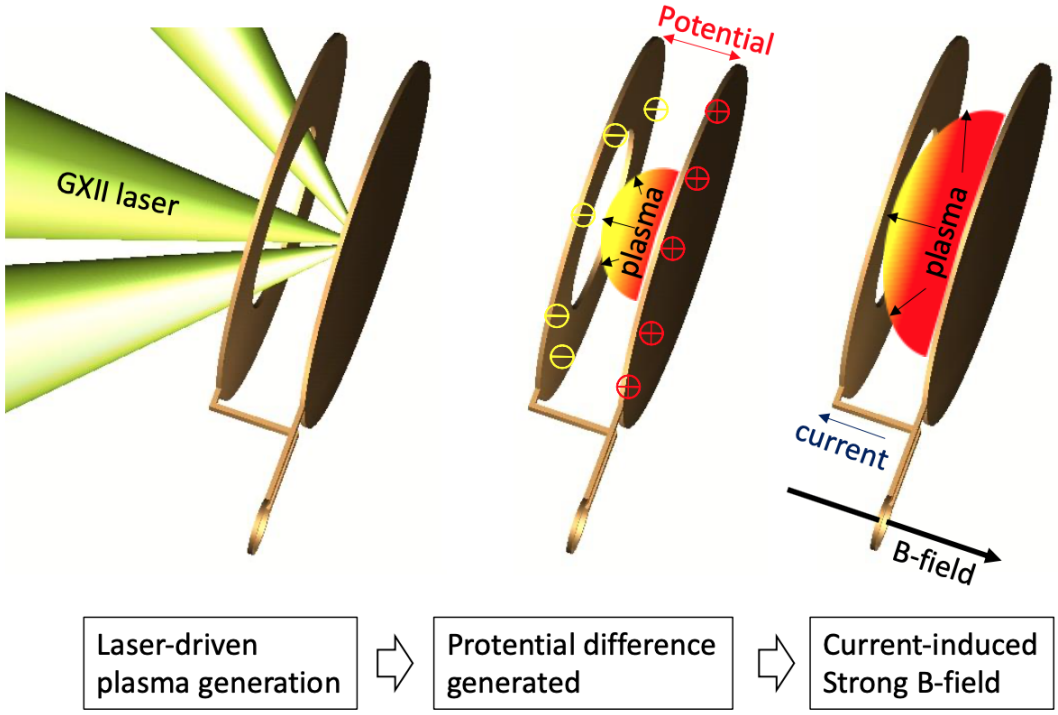

Figure 3-1: The laser driven capacitor target and the B-field generation. The plasma are generated on the rear plate, as the electrons in a plasma is moving fast than ions, the electrons arrive the front plate first. So that there is a potential difference generated between the plates and the current in the coil produces a strong B-field.

3.2 Produce a strong magnetic field in the laboratory

To generate a strong magnetic field in the laboratory, two methods are widely used in the high-intensity laser systems. One is the laser driven capacitor coil target and another one is the laser driven snail target [32–34]. In this research, the capacitor coil target is used for the strong B-field generation.

The Fig.3 − 1 shows the generation of strong magnetic field by high intensity laser. The ingenious and simple design of this target makes it widely used in the HEDP experiments, which makes it possible to generate a strength > 500T [7]. On Gekko-LFEX facility, 3 Gekko beams (kJ / ns) are used to driven a capacitor coil target. In principle, 3 Gekko beams irradiate on the back plate through the hole on the front plate which both plates are made of Nickel. The plasma is generated on the

focus spot of back plate. In plasma, as we know that the electron is moving faster than ions due to the mass difference, the electrons will attach on the front plate first. Then there is a huge potential difference between the front and back plate which will lead a current through the coil between the two plates. The current induce a strong magnetic field over 500 T through the coil.

3.3 atomic process and plasma spectrum

Discussing about the spectrum measurement, one of the most important goal in this research is to determine the basic plasma parameters [35–37]. For local thermodynamic equilibrium (LTE) and non-LTE (NLTE) plasma, there are several methods to measure the plasma electron temperature (T_e) and electron density (n_e) [38–40]. All most all of these methods need several properties of spectrum, such as line intensity and broadening.

3.3.1 The measurement of plasma temperature

For many cases of HEDP experiments, which the plasma is generated by the direct irradiation with high-power laser, the plasma is in LTE status, which can be judged by the McWhirter criterion [41]:

$$n_e \geq 1.6 \times 10^{12} {T_e}^{1/2} (\Delta E)^3 \tag{3.1}$$

where $n_e(cm^{-3})$ is the electron density and $T_e(K)$ is the plasma temperature and $\Delta E(eV)$ is the difference in the energy between the upper and lower state of all the investigated transitions.

The LTE status plasma has a simple way to estimate the electron temperature with line intensity ratio. Derived by the Saha equation [42], we have

$$T_e = \frac{E_2 - E_1}{k \cdot ln(\frac{I_1 A_2 g_2 \lambda_2}{I_2 A_1 g_1 \lambda_1})} \tag{3.2}$$

where the E_n is the energy difference of transition of the spectra from a same element, k is the Boltzmann constant, I_n is the line intensity, A_n is the Einstein coefficient, g_n is the statistical weight and λ_n is the spectra wavelength.

For NLTE plasma, for example the electron density (n_e) is in the region of $10^9 cm^{-3} < n_e < 10^{14} cm^{-3}$ where the plasma is in collisional-radiative (CR) model, the Saha equation is not available. In this region the plasma behaviour is more complex, the excitation and de-excitation processes for all states in the atom, molecule or ion have to be balanced by the population model. The detailed discussion of the exciting status of population in CR model will discussed in Chap. 5, for now we just introduce one of the methods to measure T_e in CR model, the line broadening method.

Basically, for a spectrum there are several broadening mechanisms [43]:

1. Natural broadening is caused by the finite lifetime of excited states and can be determined from the Heisenberg uncertainty relation

$$\Delta E \cdot \Delta \tau \geq h/2\pi \tag{3.3}$$

   where the $\Delta\tau(p)$ is the lifetime of state p due to spontaneous emission is called the natural lifetime.

2. Resonance broadening is caused by collisions of radiating hydrogen atoms with other hydrogen atoms of the same species.

3. van der Waals broadening ($\Delta\lambda_W$) is caused by the presence of atoms of a different kind than those of the emitting hydrogen particle. this gives the following expression for the FWHM

$$\Delta\lambda_W = \frac{5.521}{T_h^{7/11}} P \tag{3.4}$$

   where T_h is the background temperature of the heavy particles and P is the background pressure.

4. Instrumental broadening ($\Delta\lambda_I$) is caused by the instrument resolution with a

Gaussian shape.

5. Doppler broadening ($\Delta\lambda_D$), caused by the velocity distribution of the emitting particles. The intensity distribution of a Doppler-broadened spectral line has a Gaussian shape of which the full-width gives

$$\Delta\lambda_D = 7.16 \times 10^{-7}\lambda_0\sqrt{T_e/A} \tag{3.5}$$

where A is the atomic mass of the emitter expressed in a.m.u., T_e is in K and λ_0 the center wavelength of the spectra in nm.

6. Stark broadening ($\Delta\lambda_s$) is related to the plasma electron density (n_e) with a Lorentzian profile, we will discuss about it in the next subsection.

Considering about all the broadening mechanisms above in a plasma, it is possible to calculate the electron temperature by Doppler broadening width with Eq.3.5. We can use this method to estimate the T_e both in the LTE and NLTE plasmas.

3.3.2 The measurement of plasma electron density

As it is already mentioned in the subsection 3.3.1, there are several line broadening mechanisms affect on the spectra widths. Two of the most important information, T_e and n_e are both can be derived from the line width measurement if one can separate different widths components.

We already know that the T_e can be calculated by the Doppler broadening width with Eq.3.5. Considering about the plasma electron density T_e, if we know the Stark broadening width the n_e can also be obtained. To calculate the plasma electron density from the line broadening profile needs to know the element properties. As an example, for hydrogen plasma it gives

$$n_e = \sqrt{(\frac{\Delta\lambda_S}{7.4 \times 10^{-19} Z_p(\lambda_0^2)(n_i^2 - n_f^2)})^3} \tag{3.6}$$

where Z_p is the charge of the ion, n_i and n_f is the principle quantum number of the beginning and ending states.

In principle, if one knows all the factors of spectra line broadening effects and considering every components carefully, it is possible to get the plasma parameter by $\Delta\lambda_D \sim \sqrt{T_e}$ and $\Delta\lambda_S \sim n_e^{2/3}$. To separate the different line broadening profile need the deconvolution method, it will be detailed introduced in the experiment section.

Chapter 4

The Zeeman splitting measurement

In this Chapter, the first part of the EUV project which is the laboratory astrophysics study in this thesis is introduced. Pervious HEDP experiments which are focusing or relating to the strong magnetic field generation with high power laser has confirmed the existence of laser-induce field. The field is confirmed and measured with difference diagnostics, such as B-dot probe, Faraday rotation and proton photography. However, one of the most basic physical phenomenon, the spectral Zeeman splitting in the magnetic field has never been successfully observed in the HEDP experiments. The problem may be because of the theoretical guidance or experimental design, but it becomes a dark cloud shroud over the HEDP experiments. There are some researches focusing on lower magnetic field (<100 T) splitting effect in visible or UV bandwidth (200-700 nm), but for more "extreme" laser plasmas (t_e>10^2 eV, n_e>10^{19} cm^{-3}), there is no experimental and astronomical observation to the best of our knowledge. The next generation high-resolution space X-ray observatory missions may provide some data. For this purpose, to build a data base and experimental benchmark of Zeeman splitting in the high field and EUV bandwidth has its necessity, when the Zeeman splitting is widely used as an astronomical tool for the magnetic field measurement.

To design such an experiment, there are not a single one of a suitable line, a relative low plasma density and a strong magnetic field can be dispensed with. The suitable line should lay in EUV bandwidth which could transmit from relative high plasma density, and the atomic processes should be well researched in spectroscopy. silica

and carbon are common used because their high element abundance in our universe. To control the plasma density, foam or gas are easy to think about working as the plasma generator. There is also a challenge of high field generation. To generate such a high field as kilo-Tesla level usually needs an ingenious experimental design and a high power laser facility. If such a strong field is confirmed in experiment, it is also a progress in the laser plasma physics. In this Chapter, the first section will introduce the astrophysics background of this research, and next section introduces a new design for the Zeeman splitting measurement and some trials. The last section will talk about some trials which focus on the Zeeman splitting observation that the author has taken part into.

4.1 The compact star and the spectrum observation

A compact star (or compact object) refers collectively to white dwarfs, neutron stars, and black holes in astronomy. It would grow to include exotic stars if such hypothetical, dense bodies are confirmed to exist, or become a black dwarf when the energy is exhausted by radiation. All compact objects have a high mass relative to their radius, giving them a very high density, compared to ordinary atomic matter. Compact stars are often the endpoints of stellar evolution, and are in this respect also called stellar remnants. The state and type of a stellar remnant depends primarily on the mass of the star that it formed from. The ambiguous term compact star is often used when the exact nature of the star is not known, but evidence suggests that it has a very small radius compared to ordinary stars. A compact star that is not a black hole may be called a degenerate star. On 1 June 2020, astronomers reported narrowing down the source of Fast Radio Bursts (FRBs), which may now plausibly include "compact-object mergers and magnetars arising from normal core collapse supernovae" [44].

The usual endpoint of stellar evolution is the formation of a compact star. Most stars will eventually come to a point in their evolution when the outward radiation pressure from the nuclear fusions in its interior can no longer resist the ever-present

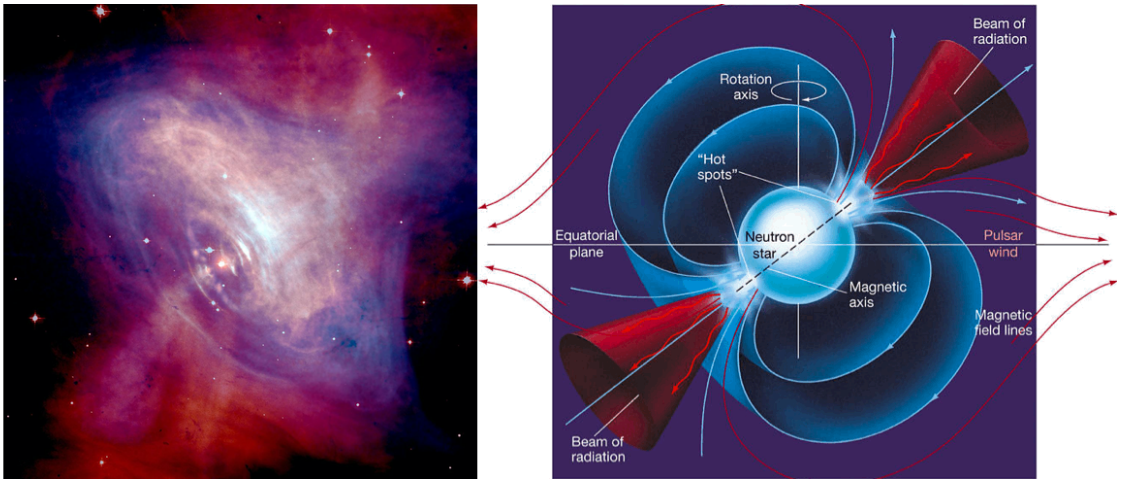

Figure 4-1: The X-ray image of Crab nebula, a pulsar is in the center of it. The X-ray image shows more details of magnetic field has influences its appearance of bipolar jet and plasma accretion disk. Indicating that magnetic field is one of the most important factors for the compact star physics. (Source: Chandra X-ray Observatory, NASA, USA)

gravitational forces. When this happens, the star collapses under its own weight and undergoes the process of stellar death. For most stars, this will result in the formation of a very dense and compact stellar remnant, also known as a compact star (Fig.$4-1$).

The compact stars have extreme strong magnetic field, for a white dwarf, the typical field strength can be 100 T, where a neutron star (or a pulsar) may achieve 10^4 to 10^11 T [45, 46]. The compact stars has the strongest magnetic field which we have observed in the nature, the characters of mater in such an extreme states must be interesting and be known very little. Now, as the technology developing the high power laser facility in the laboratory gives human a possibility to re-produce such a state on the earth. There must be more findings in the future.

Basically, the field strength on a compact star is usually beyond the laboratory capability. In this situation the non-linear Zeeman effect is possible to be observed from the astronomical data which is shown in Fig.$4-2$ [47]. The criterion is roughly at 6 kT. It means that if one can produce a magnetic field over 6 kT there may be a possibility of non-linear Zeeman effect in a laboratory by spectrum.

What One Can Learn from Studying Spectrum? Essentially all information about astronomical objects outside the solar system comes through the study of electromag-

netic radiation (light) as it reaches us. This light can contain much detailed information which is only obtained by careful analysis. Generally speaking, one can classify the information obtained by observing light according to the spectral resolution; that is the degree of sensitivity to different wavelengths, used to make the observation. One can classify such observations using the following general categories.

The most detailed astrophysical information is only obtained from high-resolution studies which involve detecting the light arriving at the earth as a function of its component wavelengths. This allows detailed spectroscopic features to be identified separately from broad band features such as color. At the highest resolution, such studies not only yield the central wavelength of any feature, often referred to as a line, but also the shape of the feature. Such studies can yield significant extra information and this thesis is largely devoted to the physical basis of this information and how it can be interpreted.

To interpret an astronomical spectrum, one needs considerable knowledge of atomic and molecular physics. This knowledge usually comes from laboratory studies which provide the basic physical parameters necessary for understanding the astronomical spectrum. There is a direct relationship between these physical parameters and the astronomical information that can be obtained by observing spectra. Thus for any line observed in an astronomical spectrum, one can potentially use laboratory data to extract the following information [48].

1. The composition of the object being observed can be inferred by knowing which atom (or ion or molecule) produces the observed transition.

2. The temperature and other physical conditions can be deduced from assigning the actual transition being observed to precise energy levels in the atom.

3. The abundance of the species undergoing the transition can only be determined if the intrinsic strength of the transition being observed is known. Line strengths can be hard to determine in the laboratory.

4. The motions of the species being observed relative to the earth, or indeed the

whole region containing the species, lead to a shift in the wavelength of the line; this shift is known as the Doppler shift.

5. The pressure or density of the environment local to the species under- going the transitions can be monitored by observing the line profile. Such observations require particularly high resolutions.

6. Any magnetic field present can be monitored as certain spectral lines will be split into more than one component. Energy levels of states which possess angular momentum are split in the presence of a magnetic field. The result is that a single transition can become two or more distinct transitions. The degree of separation between these component lines depends directly on the strength of the local magnetic field. Such splittings, if observed, can therefore provide a measurement of this field.

The information obtained from such observations is the key to most astronomical knowledge. However, to interpret any astronomical spectrum requires detailed information about the intrinsic properties of atomic spectra. Actually, we can see that the physics processes behind the spectrum properties and formation in astronomy and the atomic physics are the same. This is also the key which we can use to reproduce the astronomical phenomena and detect it with experimental methods.

4.2 Numerical simulation of plasma parameters

In order to achieve appropriate experimental conditions, there are two important issues that must be considered. The first issue is that the maximum magnetic field in the compression core should be more than 6 kT, for which the nonlinearity of the Zeeman effect becomes important for hydrogen atoms [9]. The second issue is that the electron temperature and density of the compressed plasma should be in suitable ranges for EUV line emission. This is important to produce detectable EUV spectra and to minimize the Stark line broadening effect.

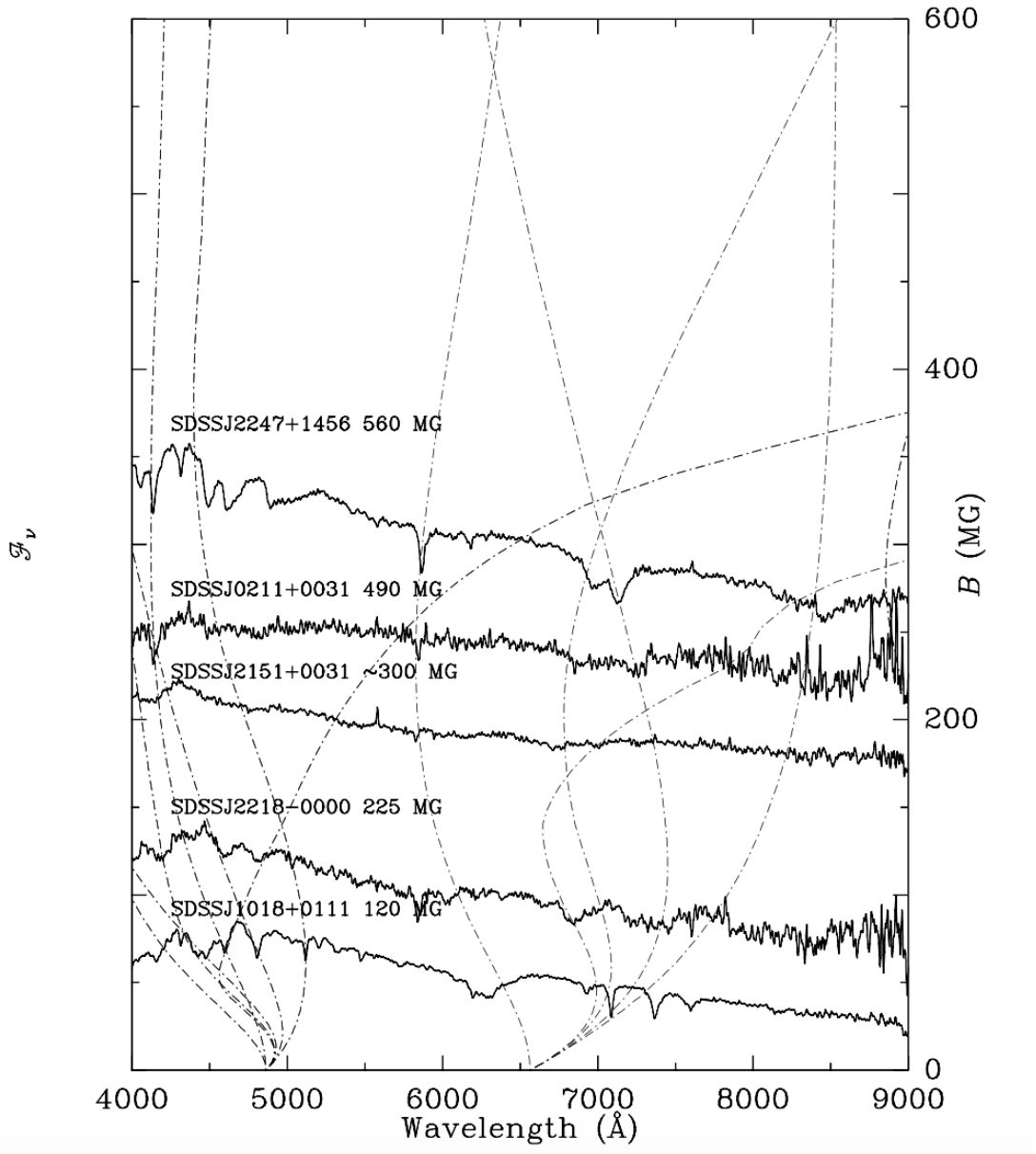

Figure 4-2: Magnetic white dwarfs fwith polar field strengths $B = 10-50$ kT (100-500 MG), compared to those components of the Balmer series that undergo turnarounds or reach stationary points in the region of interest. Spectra are positioned along the ordinate by the approximate mean surface field strength.

We use the FLASH code to calculate the two-dimensional (2D) plasma hydrodynamics under an external magnetic field. FLASH is a modular, parallel, multi-physics simulation code that is capable of handling general compressible flow problems found in many astrophysical environments [49] and high-energy-density-physics systems [50]. In addition, the magnetic field effect is included in the FLASH code. The Zeeman splitting can be more easily observed at longer wavelengths. However, long wavelength light is absorbed in high-energy-density-plasma due to its high opacity. EUV light is better for Zeeman spectroscopy in high-energy-density plasma. The plasma parameters obtained from the FLASH calculation can be used to test and verify the spectrum in a simulation.

Using these results, we were able to identify experimental conditions appropriate for the Gekko-XII experiment. A 250-μm radius and 10-μm-wall-thickness plastic cylinder tube is filled with a 1-mg/cm^3 SiO_2 foam. The foam density is determined not only by simulation results but also by its availability [51]. The cylinder surface was irradiated with laser beams having 10^{13} W/cm^2 of peak intensity and a 1.2-ns full-width-at-half-maximum (FWHM) Gaussian pulse shape. The laser intensity peaked at 2.0 ns in the simulation time. As mentioned earlier, the seed magnetic field should achieve a maximum strength when the foam compression begins. In the real experiment, the field driven laser is applied 1 ns before the compression starts. In the simulation we set a parallel seed field at the initial timing, which is sufficient for the calculations.

We performed the magneto-hydrodynamic simulation with and without the seed magnetic field parallel with the cylinder axis. We found that the Zeeman effect is related to the angle between the magnetic field and the observational direction, and we chose the seed field based on this and set the spectrometer parallel to the cylinder axis. The strength of the seed field was set to be 100 T, which is easily achievable with the capacitor-coil target [6]. Fig.4$-$3(a) shows the 2D hydrodynamics of a laser-driven cylinder calculated with the FLASH code. (a) is the initial state of the foam filled cylinder target (0 ns). The simulation results show that the maximum compression occurs at 3.1 ns. Fig.4 $-$ 3 (b) and (c) show the mass density profiles (g/cm^3) at the

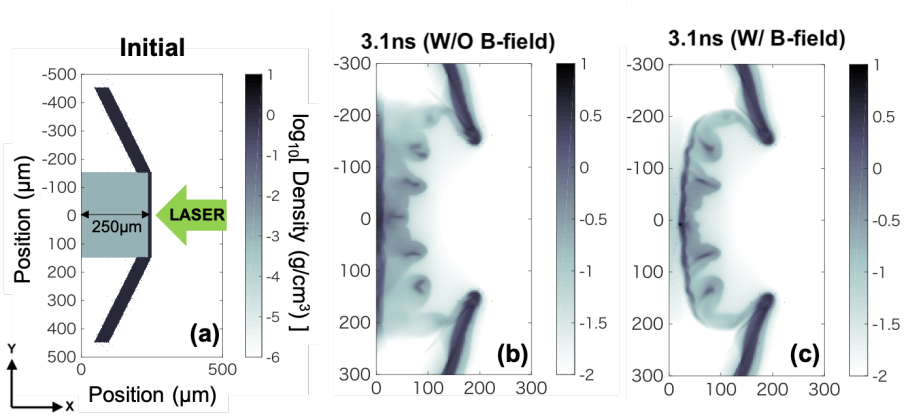

Figure 4-3: 2D hydrodynamics calculated with the FLASH code.(a) Initial state of the foam filled cylinder target (0 ns). (b), (c) Mass density profiles at the maximum compression time (3.1 ns), without and with the seed magnetic field, respectively. The seed magnetic field is parallel to the cylinder axis.

maximum compression time (3.1 ns) without and with the seed magnetic field (the seed magnetic field is parallel to the cylinder axis), respectively.

At the maximum compression timing, the magnetic field pressure is important for terminating the plasma and field compressions [52]. The diameter of the compressed core with the seed magnetic field is about two times larger ($\sim$ 25 μm) than that without the seed field.

The plasma β is defined as the ratio between the sum of the plasma thermal pressure ($P_{\rm therm}$) and plasma dynamic pressure ($P_{\rm dyn}$) and the magnetic field pressure ($P_{\rm B}$):

$$\beta = \frac{P_{\rm therm} + P_{\rm dyn}}{P_{\rm B}} = \frac{n_{\rm e} k_{\rm B} T_{\rm e} + \frac{1}{2}\rho v^2}{B^2/2\mu_0}, \tag{4.1}$$

where $n_{\rm e}$ is the number density of electrons, $T_{\rm e}$ is electron temperature, $k_{\rm B}$ is Boltzmann constant, ρ is plasma mass density, v is plasma bulk velocity, B is magnetic field strength, and μ_0 is permeability. Fig.$4-4$ shows 2D profiles of: (a) the electron density ($n_{\rm e}$), (b) electron temperature ($T_{\rm e}$), and (c) magnetic field strength (B) at the maximum compression timing (3.1 ns). The magnetic field strength, electron density, and electron temperature are, respectively, 12 kT, $1.6 \times 10^{21}/{\rm cm}^3$, and 103.4 eV at the central area. Clearly, a higher density increases the electron density and makes

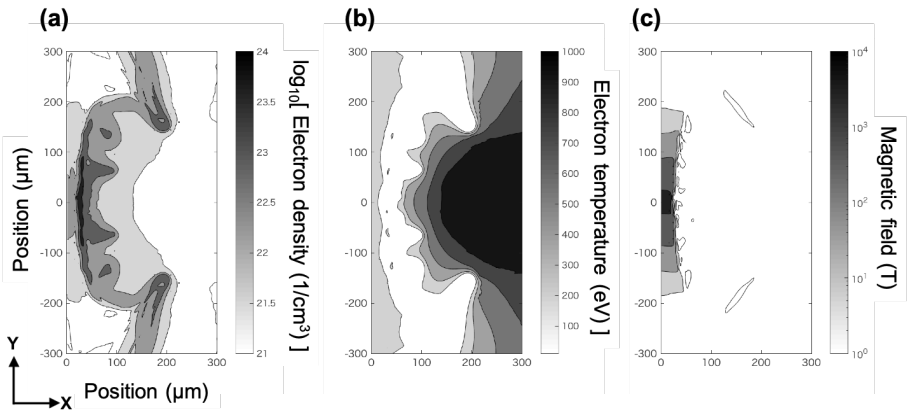

Figure 4-4: Two dimensional profiles of the key plasma parameters at the maximum compression timing. (a) Electron density (n_e, in log_{10} /cm^3) profile. (b) Electron temperature (T_e, eV) profile. (c) Magnetic field strength (B, T) profile

Table 4.1: Parameters for different foam compressions

ρ_{foam}	n_e	T_e	B_{max}
1 mg/cc	1.6×10^{21}/cm^3	103.4 eV	12 kT
5 mg/cc	7.5×10^{22}/cm^3	129.3 eV	11.4 kT

the Stark effect more effective, and also changes the temperature. Table 1 shows the FLASH code calculation results for a higher density 5-mg/cc foam. The Zeeman splitting and Stark effect are not as effective due to the relatively low electron density at the maximum compression timing, demonstrating why a 1-mg/cc foam was chosen. Of course, a lower density gives a lower electron density, which will be a challenge for the target technicians.

At the maximum compression timing, $P_B = 0.4$ Gbar. Fig.$4-5$ shows the 2D β profile at the maximum compression timing, showing that the central area reaches a pressure equilibrium $\beta = 1$ at the maximum compression timing.

The energy width between lines separated by the Zeeman effect can be obtained with plasma parameters calculated with the FLASH code. The nonlinearity of the Zeeman effect becomes significant for hydrogen atoms in a 6-kT magnetic field. However, the linear model is still applicable for calculating the energy width for silicon atoms in a magnetic field as strong as 10 kT, expected in our experiment. The EUV and VUV spectrometers used for the spectral measurements cover wavelengths of

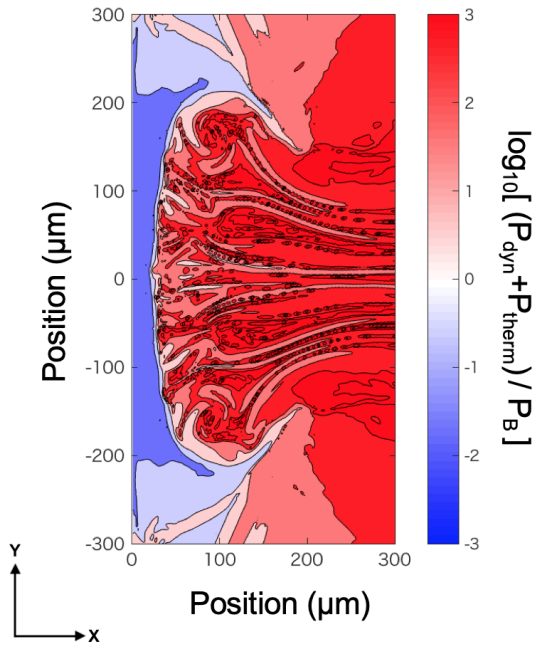

Figure 4-5: Two-dimensional β value at the maximum compression time (3.1 ns).

10–200 nm, corresponding to photon energies of 6–120 eV. There are many potential lines that can be used for the Zeeman splitting measurement in such a wide range. We identified the Si XII (Lithium-like) line at 95.4 eV as being an appropriate choice for measurements in the definite plasma condition.

The linear Zeeman splitting model gives

$$\Delta\nu = \frac{\mu_{\mathrm{B}} \cdot B(m_1 g_1 - m_2 g_2)}{h}, \tag{4.2}$$

where $\Delta\nu$ is the frequency difference caused by the Zeeman effect, μ_{B} is the Bohr magneton, m and g are the magnetic quantum number and Landé g-factor of the electron state, and h is the Planck constant [53]. The maximum energy shift is calculated to be 3.4 eV for the emission line at 95.4 eV under a 10-kT magnetic field. However, a 10-kT magnetic field is strong enough to destroy the $L + S$ coupling and lead to the splitting being Paschen–Back effect dominant [54], resulting in a different pattern of splitting. In a relative weak magnetic field, the coupling of the orbital angular momentum L to the spin angular momentum S is stronger than their

coupling to the external field, which means that $L+S$ coupling is dominant. In a 10-kT strong magnetic field, L and S coupling is stronger to the external magnetic field than the coupling to each other, and can be visualized as independently precessing about the external magnetic field direction. The energy shift of the Paschen–Back effect gives

$$\Delta E = (m_l + m_s)(\frac{ehB}{2m_e}) = (m_l + 2m_s)\mu_B B \tag{4.3}$$

which is similar to the normal Zeeman effect but only two splitting lines can be observed [55]. In addition, a consideration of the selection rules of electric dipole radiation gives

$$\Delta J = 0, \pm 1, \qquad \Delta M = \begin{cases} \pm 1, \sigma \ components, \\ 0, \pi \ components, \end{cases} \tag{4.4}$$

where M is the magnetic quantum number. By observing along the magnetic field direction, which means that the light coming into the diagnostic system is parallel to the seed field, the σ components acquire a circular polarization and the π components disappear. That is why we set the EUV and VUV spectrometers along the magnetic field in the experimental design. Finally, in the 10-kT magnetic field the maximum splitting in the σ components is calculated to be 1.2 eV.

For non-hydrogenic ions, the Stark broadening occurs predominantly by electron impact [56]. Since the perturbations caused by ions is negligible compared to electrons, it can be calculated as $\Delta\lambda_{s1/2} = 2W(n_e/10^{16})$, where W is the electron impact parameter, which can be calculated for different temperatures [57]. It can be calculated that the Stark broadening corresponds to an energy of 0.7 eV, which is smaller than the Zeeman splitting width for an electron density of 10^{21} cm^{-3}.

The EUV spectra were calculated using the FLYCHK code [58] and the splitting profile was calculated by the MASCB-PPPB code [59], in which the Stark effect is considered as line broadening, with the plasma parameters obtained from the FLASH result. As described in the pervious discussion, the compressing core has parameters of about B = 10 kT, $n_e = 10^{21}/\text{cm}^3$, and T_e =100 eV at the maximum compression

timing. The calculated spectra with the above plasma parameters are shown in Fig.4−6. EUV spectra calculated by the MASCB-PPPB code with plasma parameters calculated with the FLASH code at the maximum compression timing. The black line is the spectrum of the Si XII line (Li-like), observed as being isotropic. The blue line is the π-component dominated line (perpendicular observing) and the red line is the σ-component dominated line (parallel observing). A 1.2-eV splitting along the magnetic field is apparent where the σ components dominate. The emission peak near 95.4 eV comes from Lithium-like silicon ions (Si XII) by the transition between $1s^2 4f$ and $1s^2 3d$. However, in the actual experiments, the resolution of the spectrometer must be considered. For this purpose, a spectral convolution is also calculated, as shown in Fig.4 − 7. These spectra were obtained by convoluting the spectral result with a spectral resolution function of a 1-eV resolution EUV spectrometer. The black line is without a magnetic field, and red line is in a 10-kT external magnetic field with σ components. The splitting is not as apparent even if we observe it along the cylinder axis, using a minimum 1-eV resolution spectrometer, but a 0.5-eV splitting can still be observed for our high-resolution spectrometers for the best experimental conditions. High-resolution spectrometers will achieve a better spectrum. In conclusion, the Zeeman splitting is observable in this plasma condition even considering the Stark effect and spectrometer resolution.

4.3 Experimental design and diagnostic setting up

Fig.4 − 8 shows a schematic drawing of the design of the experimental setup. A cylindrical plastic tube of 20-μm thickness filled with a low-density SiO_2 foam is the main target. The plastic cylinder, located at the center of the two capacitor coil targets, is compressed by six Gekko-XII laser beams. The SiO_2 foam in the cylinder tube becomes a strongly magnetized SiO_2 plasma by laser-driven implosion. EUV/VUV lines emitted from magnetized Si ions are split by the Zeeman effect and observed with a high-spectral-resolution EUV/VUV spectrometer along the cylinder axis. Silicon is selected as the target atom because it is one of the most abundant

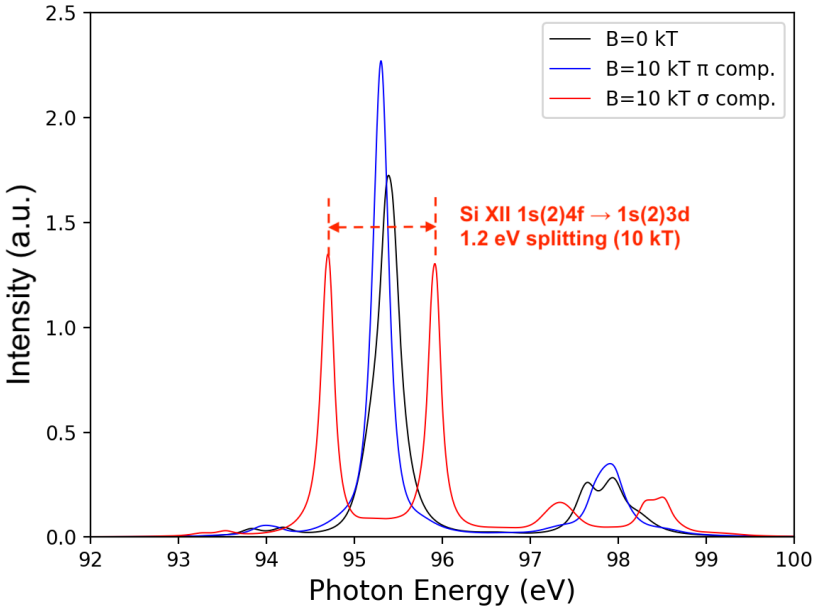

Figure 4-6: EUV spectra calculated by the MASCB-PPPB code with plasma parameters calculated with the FLASH code at the maximum compression timing. The black line is the spectrum of the Si XII line (Li-like), observed as being isotropic. The blue line is the π-component dominated line (perpendicular observing) and the red line is the σ-component dominated line (parallel observing).

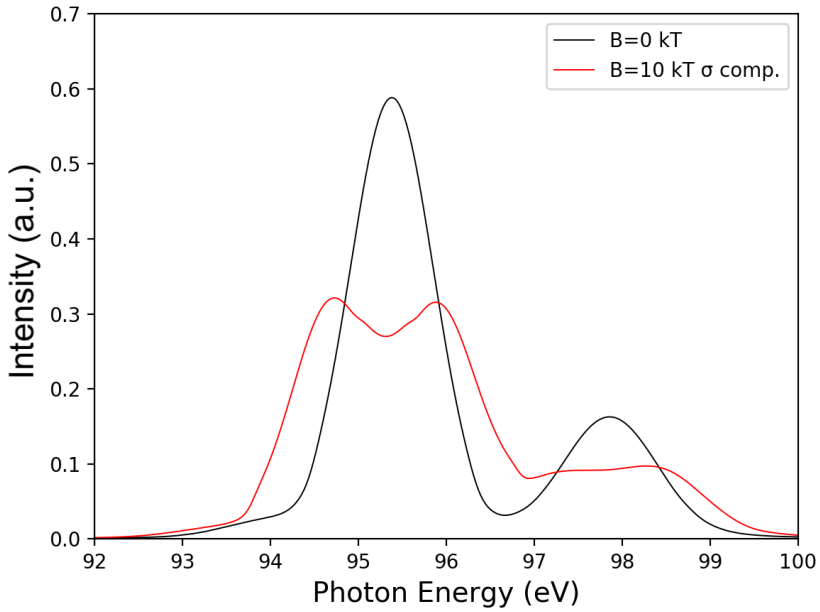

Figure 4-7: 1-eV convolution spectrum results of the Si XII line at 95.4 eV, without a magnetic field (black line) and in a 10-kT external magnetic field, with σ components (red line).

elements in the universe [15]. Silicon ion emission lines are frequently observed in astronomy. The low-density SiO_2 foam is used to reduce the Stark broadening effect [60,61]. If the Stark broadening is wider than the Zeeman splitting energy, the Zeeman splitting is smeared by the Stark broadening. Based on calculations, we chose a 1-mg/cc density foam for the experiment as appropriate for measurement. As there may be stray light irradiating the two ends of the cylinder and causing foam heating, two CH cones are attached to the ends of the cylinder to block stray light. The cylinder is placed in a spatially uniform seed magnetic field produced by a pair of laser-driven capacitor-coil targets. A 20-μm thick tantalum shield is attached to each coil to prevent the X-rays from the laser spots irradiating the cylinder. A $\sim 10^2$-level seed magnetic field is generated by two Gekko-XII beams (one beam is used for each coil). In a previous experiment, a capacitor-coil target was irradiated by one Gekko-XII beam and generated a 250-kA current and 610-T magnetic field at the center of the coil [7]. Using two capacitor-coils generates a stronger magnetic field [62].

The cylinder is soaked in the generated magnetic field before the laser irradiation.

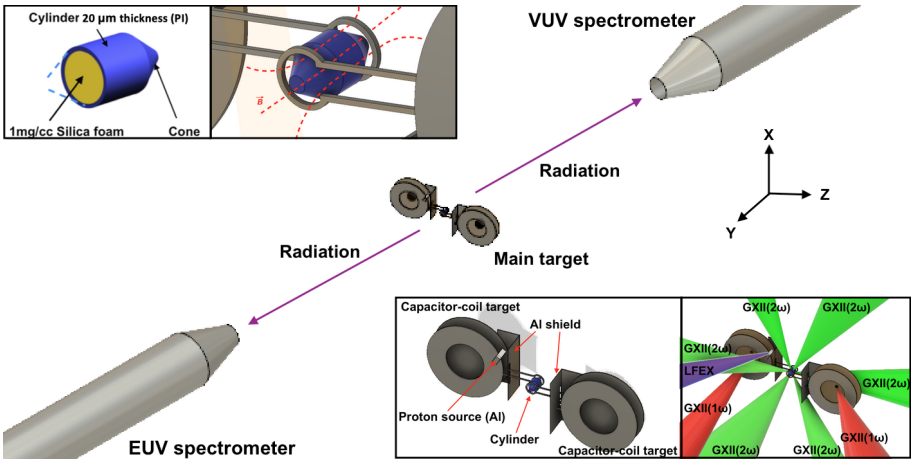

Figure 4-8: The Zeeman measurement experimental setup. The plastic cylinder, located at the center of the two capacitor coil targets, is compressed by six Gekko-XII laser beams. The SiO_2 foam in the cylinder tube becomes a strongly magnetized SiO_2 plasma by laser-driven implosion. EUV/VUV lines emitted from magnetized Si ions are split by the Zeeman effect and observed with a high-spectral-resolution EUV/VUV spectrometer along the cylinder axis.

The main target is then irradiated by six Gekko-XII beams, which drive a cylindrical shock wave in the SiO_2 foam. The magnetic field seed is compressed by a converging flow of highly conductive SiO_2 plasma produced by the converging shock wave. The magnetic field driven beams are applied 1 ns before the six Gekko-XII compression beams, in order to get the maximum seed field when the compression starts. At the maximum compression timing, the hot SiO_2 plasma is magnetized by $\sim$ 10 kT of the compressed magnetic field. EUV spectra emitted from the magnetized silicon ions are measured with a grazing incidence EUV spectrometer coupled with an X-ray streak camera to obtain high spectral and temporal resolutions. On the opposite side, a VUV spectrometer measures the potential splitting in the VUV wave band. Both the EUV and VUV spectrometers are coupled with pinholes to obtain images of the central area of the plasma. The pinholes also shield signals from other hot plasmas, for example signals from the cylinder shell or capacitor coils heating. The hydrodynamics and magnetic field structure of the compressing cylinder are measured simultaneously by X-ray self-emission and proton radiography techniques.

The density of the SiO_2 foam and thickness of the CH cylinder must be optimized

to obtain clear Zeeman spectra in the experiment. The CH shell works not only as a container for the foam but also as a piston to drive the converging shock in the foam.

4.4 Trials of the Zeeman splitting measurement

In order to observe the Zeeman splitting in the experiment, we also performed our experiment on Gekko / LFEX system in 2018 based on the discussion above. The first subsection will introduce this experiment, and the second subsection will introduce another experiment performed on LULI facility, Ecole Polytechque, France.

4.4.1 Gekko XII / LFEX experiment

Based on the discussion in section 4.2, we performed the experiment with the similar design. There are some differences between the design and experiment.

1. Only EUV spectrometer is used in the experiment. Before the experiment the VUV spectrometer is also setup, but the front image lens (using optics, not pinhole in the design) is broken by the target debris in the first shot. And it is never used in this experiment series.

2. The proton backlight target is not set up in the following experiment, as the target-insert operator found that it is difficult to operate it in position by human hand.

3. The foam targets are fabricated by the Lawrence Livermore National Laboratory (LLNL), United States [63]. Three different density of foam targets are provided (10mg/cc, 5mg/cc and 1mg/cc), But the foam targets are very fragile and all of 1 mg/cc and some of higher density targets are lost. However, as the simulation is based on 2D, higher density may also fullfill the spectrum observing conditions.

These differences indicate that in the experiment, especially on big facilities it is never an easy work to bring the ideal setting up to the reality, what we can do is try our best to coordinate. Although the Zeeman splitting has a solid physical theory and

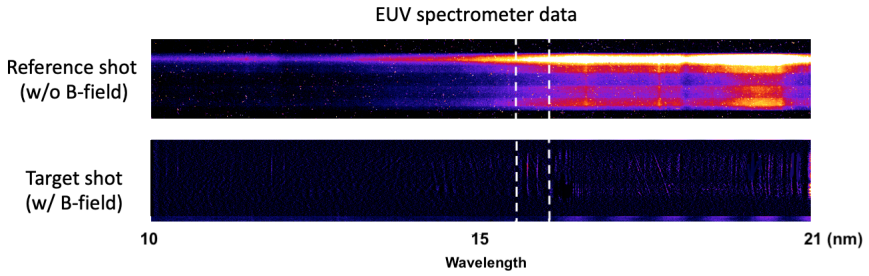

Figure 4-9: The raw data of EUV spectrometer. The upper figure is w/o B-field shot as reference one, and the lower figure is the w/ B-field shot.

should not be absent in the HEDP experiment, to observe it still need a simple and subtle experiment plan.

Here we show a raw data from EUV spectrometer in Fig.$4-9$. On the reference shot we can see two significant O V line at 17 nm ($1s^2 2s4d$ to $1s^2 2s2p$), and 18.6 nm ($1s^2 2p3p$ to $1s^2 2s2p$). Other spectrum is absent or difficult to confirm. The lower one shows the target shot with magnetic field. There is no lines corresponding to each other which can be used to compare the potential Zeeman shifting. At 16.17 nm and 16.32 nm there are a double line exist with a similar intensity. If it is a Zeeman splitting the energy difference is 0.16 nm / 0.7 eV. However, There is no line on the reference shot at same position and no known spectra at $\sim$16.2 nm so that cannot identify the element (Fig.$4-10$, where is in the white dotted line of Fig.4-7). On the target shot there is a wave shape background shape on the right side ($\geq$ 16.6 nm) of the spectrum. It is not physical but a grating failure after the post-mortem.

So that the evidences are lacking to make a solid conclusion to say there is a splitting with so many diagnostics unavailable in the experiment. The possible reason may be:

1. The plasma was not generated successfully. This is one of the decisive reasons which we guessed, the foam-fill cylinder was not compressed correctly. That may explain why only Oxygen lines were observed when the Silicon lines were missing as the Oxygen has multiple origin while Silicon has not.

2. The magnetic field did not achieve the ideal intensity, or even not generated.

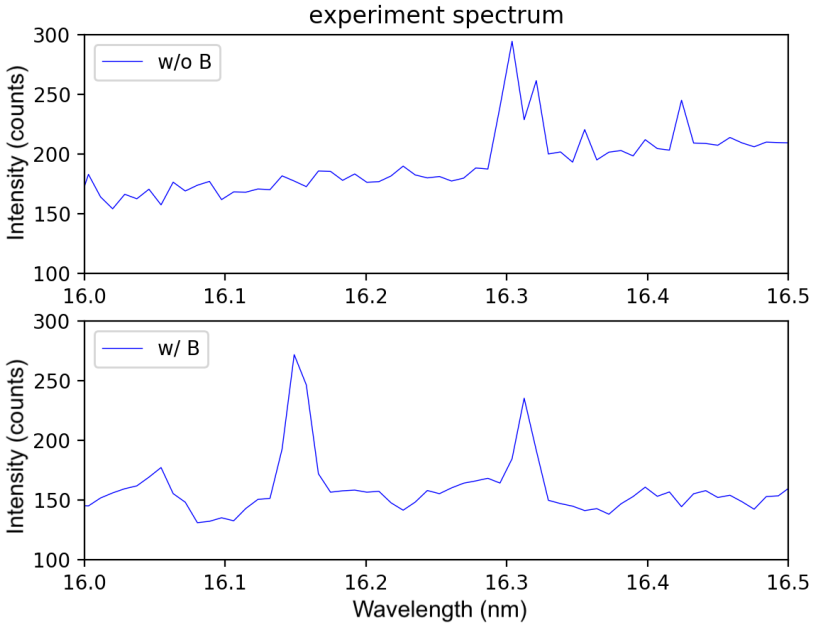

Figure 4-10: The spectra at 16nm in the experiment, there is a double-peak in the w/ field shot but there is no corresponding spectra in the reference w/o field shot. The 16.3 nm peak in w/o field shot is due to the noise spot.

> There is not significant splitting on Oxygen line indicate this possibility. Even though there is a background disturbing, there are no splitting lines overlying on it.

But this trial still provide some experiences for the Zeeman splitting measurement. Of course the plasma status and radiation properties are very important for the Zeeman splitting measurement, on the other hand, we also need to consider more about the reality. Experimental operation has so many limitations for the facility. It is necessary to try simpler design and less materials to reduce the disturbing.

4.4.2 LULI experiment

In September 2019, the author participated another Zeeman splitting measurement experiment performed on the LULI facility, Ecole Polytechque, France. Two nanosecond laser is used in this experiment. One beam is used to drive the laser-induce strong magnetic field, and another one is used to generate the low density plasma.

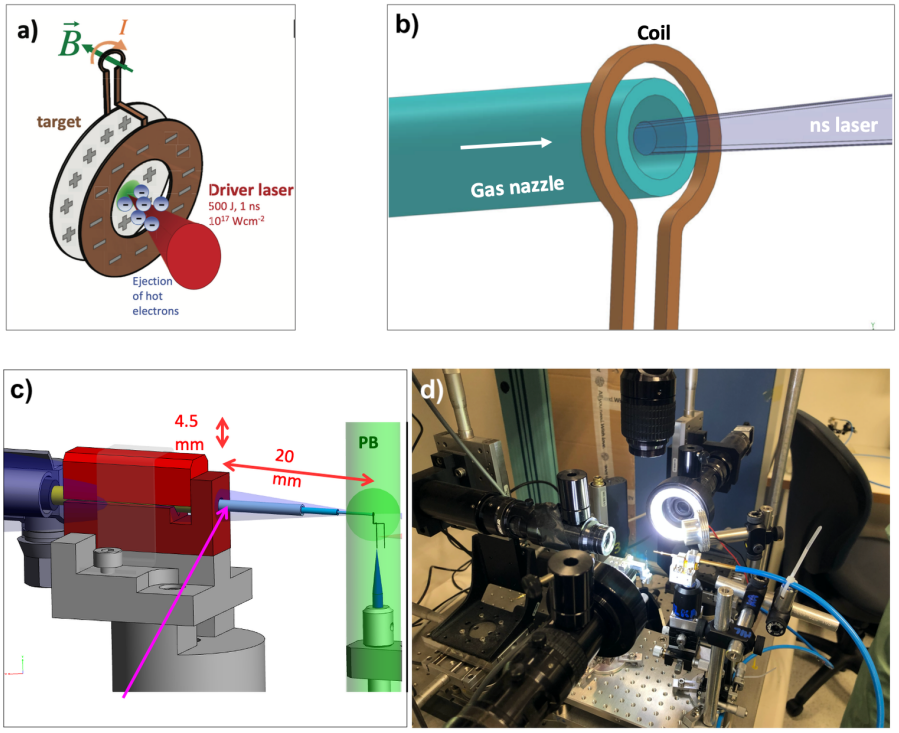

Figure 4-11: The experimental setup of LULI experiment. a) B-field generation by capacitor-coil target (1053 nm,500J ns-beam). b) CO_2 gas is ionized into plasma by 1052 nm, 50J and 500 ps-beam. c) and d) The target schematic diagram in design and realistic assembling.

The experiment setup is shown in Fig.4 – 11. The 500 T magnetic field is generated by the capacitor coil target (a), and a gas nozzle is insert into the coil, puff the CO_2 gas into the it and irradiated by another beam (b), generated a low density (about $10^{18} cm^{-3}$) plasma. According to the experimental condition there is an 2 nm splitting can be observed at one of the carbon UV spectrum (CIII 229 nm).

The diagnostic is a 1200l/mm gratings UV spectrometer with 0.2 nm resolution. The spectrometer is coupled with a streak camera so that the spectrum data can be temporal resolved as well. The experiment result is shown in Fig4-13. The x-axis is wavelength, covered 15 nm from left to right. The y-axis is time, covered 20 ns from top to bottom. The magnetic field is generated 1 ns later than the CO_2 plasma, it can be seen the CIII 229 nm line is observed in the CCD view. However, when the magnetic field generated and achieved the maximum intensity (about 1 ns after the B-field driven beam), there is no splitting observed at 229 nm spectra. The spectra

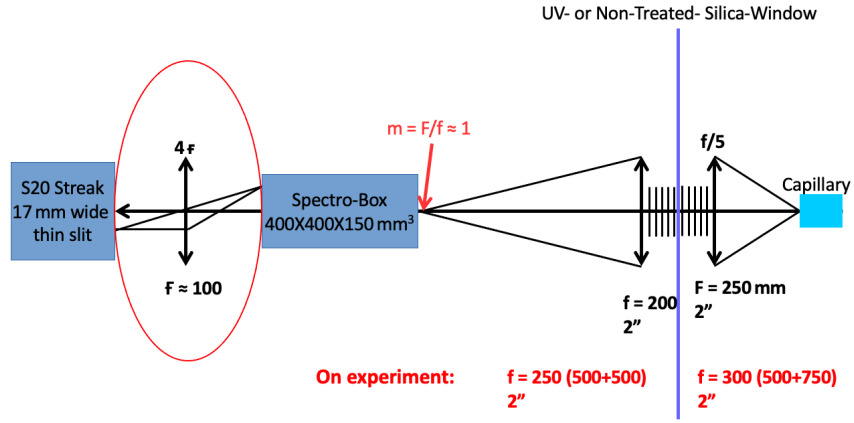

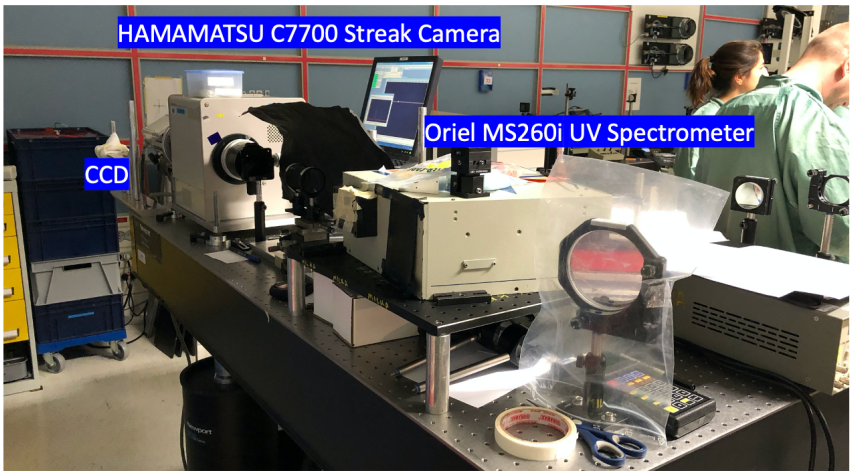

Figure 4-12: The diagnostic system of LULI experiment. The upper figure is the optical and diagnostic system and the lower one is the deployment in the experiment. The UV light is induced into streak camera (Hamamatsu C7700) coupled spectrometer (Oriel MS260i) the approximate 1:1 optical system. With 200μm slit and 2400l/mm grating it is possible to get 1 nm resolution at 230 nm UV line.

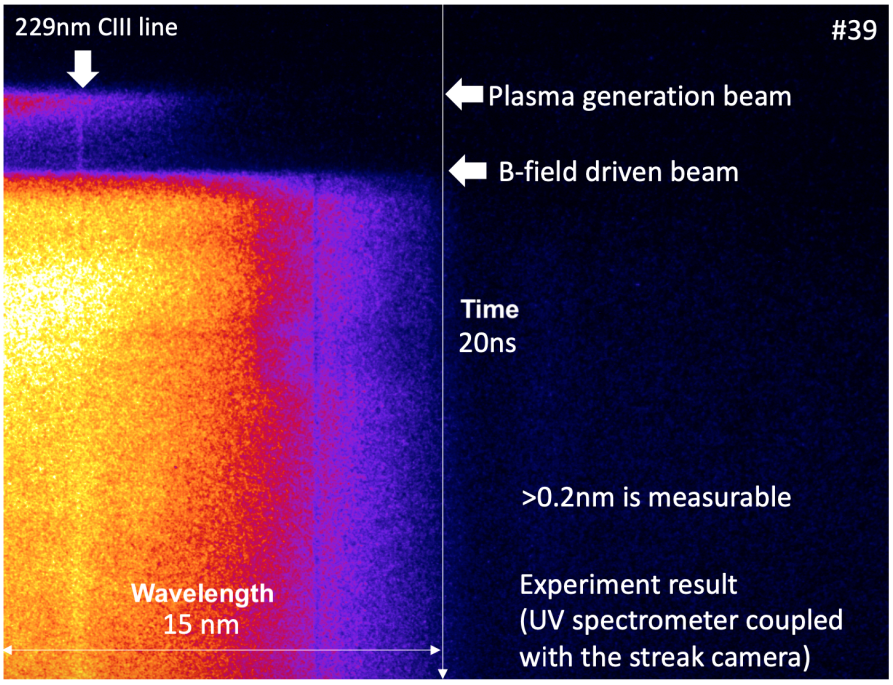

Figure 4-13: The one of the typical target shot results of LULI-Zeeman experiment. the horizontal axis is the wavelength and the vertical is time, from top to bottom. The available spectrum width is about 15 nm, and the time evolution covers 20 ns. The gas plasma is produced about 1 ns before the B-field generation.

is shown in Fig.$4-14$. There is a very tiny broadening effect at 229 nm CIII spectra, if it is due to the Zeeman effect, the field strength can not be larger than 40 T, which is much weaker than the original goal >500 T.

The possible reason to explain the Zeeman splitting absent is the magnetic field is not generated successfully. In some of the target shots, after checking the optical images of the experiment operators found that sometimes the capacitor coil is blowed away by the puffed gas, which would make the B-field driven laser miss the target. Another probably reason is that there is a short cut between the nozzle and the coil, which would lead the current miss the coil and dismiss the magnetic field.

According to these trials, it is obviously that a simpler design is necessary both for theoretical works and experiment operators. A strong magnetic field is usually produced in a relative small spatial and temporal region, but the plasma-in-field should be high temperature and low density which usually generated in a relative large spatial region. On the other hand, the observing direction is limited. These

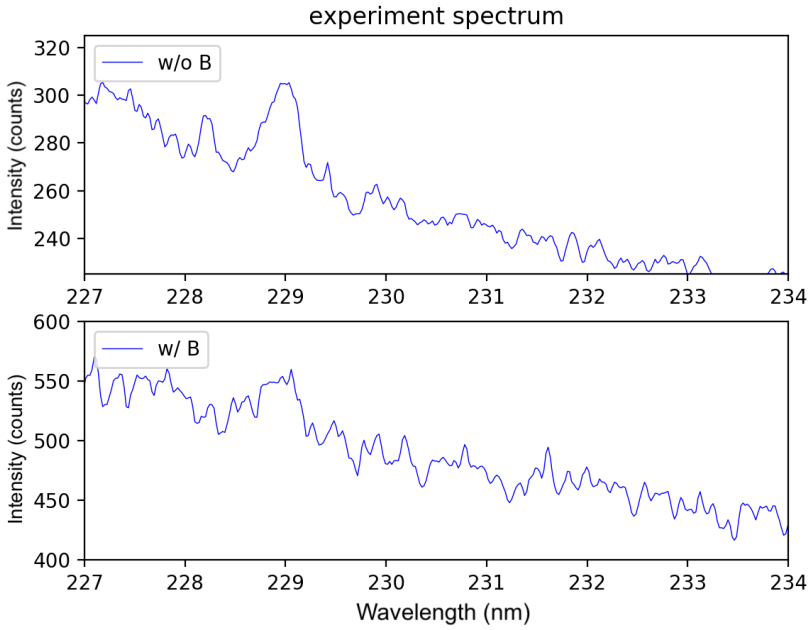

Figure 4-14: The spectrum of the the raw data shows w/o and w/ B-field. At 229 nm there is the CIII line in w/o B-field spectrum but w/ B-field case the S/N ratio decreases, and no significant splitting observed (The theoretical prediction is about 4 nm).

factors may makes the Zeeman splitting measurement to be a tricky work which we need to solve in the future HEDP experiments.

4.5 Summary of the Zeeman splitting experiment

The previous sections have mentioned that not a single one of a suitable line, a relative low plasma density and a strong magnetic field can be dispensed with. From these trials, there are still some achievement we can talk about.

1. Starting with the astronomical meanings, Si spectrum which is one of the richest elements and well-observed in astronomy researches are chosen in the HEDP experiment plan. The author picks one of the potential EUV spectra and calculates the Zeeman splitting in 10 kT strong magnetic field. This result can be a guidance for the present and future Zeeman splitting experiment with laboratory astrophysics background.

2. Aiming at observing this spectra, the author designs an experimental plan with Gekko facility, and confirms the plasma parameter is possible for the present spectroscopy science to measure such a splitting with MHD modeling.

3. The experiment needs an ultra-low density SiO_2 foam of 1 mg/cc, our collaborators from LLNL successfully fabricated it which is a good examining for the target-fabricating technology.

4. Both of the Gekko and LULI experiments observed some potential splitting, or broadening effect. In Gekko experiment, whether the spectra observed around 16.2 nm was caused by magnetic field or not, the experiment shows that the present EUV spectrometer has the acceptability for Zeeman splitting measurement in the planning condition. For LULI experiment, as the field may be much lower than the original plan, A higher resolution diagnostic system is needed for the future experiment.

Both trials of Gekko and LULI facility showed that an ingenious target design is necessary. As mentioned above there are some guessing for the reasons of the

absence of the Zeeman splitting, for future experiments to confirm the plasma status is important for analyzing the experimental data. For the foam target, a streak camera or self-emission diagnostic system can be set up to check the compressing process and compression ratio, and comparing with the 2D MHD simulation density distribution result. A proton back-lighter target is still necessary for the magnetic field cross-check measurement in this experiment.

About the CO_2 gas plasma experiment of LULI facility, a possible improvement is to increasing the coil diameter. This changing will reduce the magnetic field strength which means the researches must be carefully examining the field changes with the diameter and re-calculate the splitting width, and testing whether it is observable in the experiment.

Chapter 5

EUV project for H* measurement and atomic process

EUV light source (13.5 nm) widely used in EUVL for chip curving recent years. It has about 10 years history for processor-making industry, as a replacement, new light source technology for mercury g & i-line, KrF and ArF light source. The scientists and engineers are keep working on to find a better light source for curving chips. A shorter wavelength source can improve the lithography resolution, which means a more powerful, but smaller and energy-saving processor can be produced. In 2020, with the newest EUVL technology 5 nm level node structure of processor is achieved, which is already applied on the iPhone 12's processor "A14 Bionic" by Apple Inc. [64]. The improvement of EUV lithography technology is shown in Fig.$5-1$.

In this Chapter, the author will introduce another application of researches related to the EUV. Different from the previous Chapter, here will be more related to the industrial applications. The final goal of the project is using one of the component in EUV-induced plasma, H readical (H*) to clean the Sn ions in the Chamber when the Sn is used as the EUV source. The laser heating Sn is common used as the EUV source in EUVL, but the Sn debris are easy to attach on the EUV reflect mirror, and decrease the reflecting efficiency gradually. In the EUVL, a widely used method to slow down this process is inducing H_2 as a buffer between Sn debris and mirror. An interesting thing is the technicians and engineers noticed that when they are inducing

the H_2 into the chamber, the mirror life is significant extended which is beyond the buffer mechanism. Some researchers suggest that H* play an important role in this effect. This research will try to observe the EUV-induce hydrogen plasma parameters, and try to estimate the H* yield [65, 66]. The next step is try to find the possibility of applying this technology to Sn cleaning [67, 68]. The first section introduces the EUV-induce hydrogen plasma spectrum measurement, especially the Balmer series for the key plasma parameters (T_e and n_e) estimation. The second section provides the methods of H* estimation. The last section will give a discuss about the probably applications.

As the previous description the experiment setup is shown in Fig.$2-3$, here we provide a raw data of the H-Balmer series which we obtained from the experiments. In the experiments the first three lines of Balmer series are observed which are shown in Fig.$5-2$. Obviously, the H_α and $H_\beta$line has better S/N ratio, and H_γ one is worse than the others.

In the section 3.3, we discussed how to derive the key plasma parameter from the spectra profile. Obviously, this method demands a good S/N ratio. Considering this factor, the H_α and H_β line should be good choices. But for hydrogen plasma diagnostics, usually, H_β profile are used for the broadening measurement [69, 70]. That is because the H_β line is more sensitive to the Stark broadening than the H_α line. That means when we talk about the line broadenings, H_α is Doppler broadening dominated while H_β is Stark broadening.

According to our experimental parameters, the pressure of hydrogen gas we pumped into the gas cell is relative low (1-10 Pa) which means that the van der Waals broadening is very small [71]. Actually for H_β line profile, the natural, resonance and van der Waals broadening are all at least 2 orders smaller than the other 3 broadening mechanisms. So that when we analyzing the experiment data only Doppler broadening ($\Delta\lambda_D$), Stark Broadening ($\Delta\lambda_S$) and Instrumental broadening ($\Delta\lambda_I$) are taking into account. As the Doppler and Instrumental profile has a Gaussian shape ($G(x, \Delta\lambda_G)$) and Stark Broadening has a Lorentzian profile ($L(\lambda_0 - x, \Delta\lambda_L)$), the total line shape

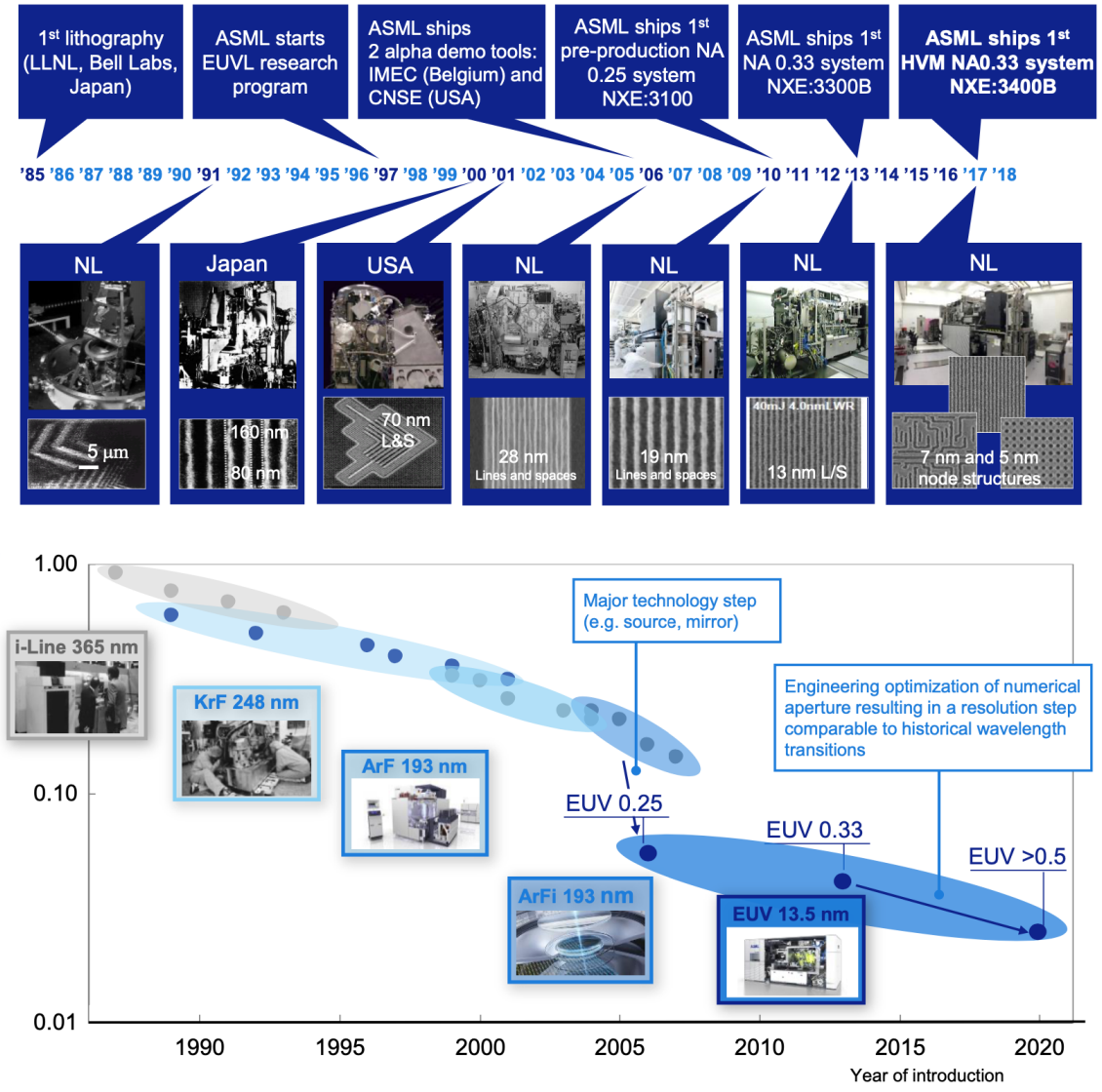

Figure 5-1: The history of light source development of EUVL technology and resolution relative improvement. The scientists and engineers are keep working on to find a better light source for curving chips. A shorter wavelength source can improve the lithography resolution, which means a more powerful, but smaller and energy-saving processor can be produced. In 2020, with the newest EUVL technology 5 nm level node structure of processor is achieved. (Source: I. Fomenkov, ASML, NL)

5.1 Spectrum measurement of EUV-induced hydrogen plasma

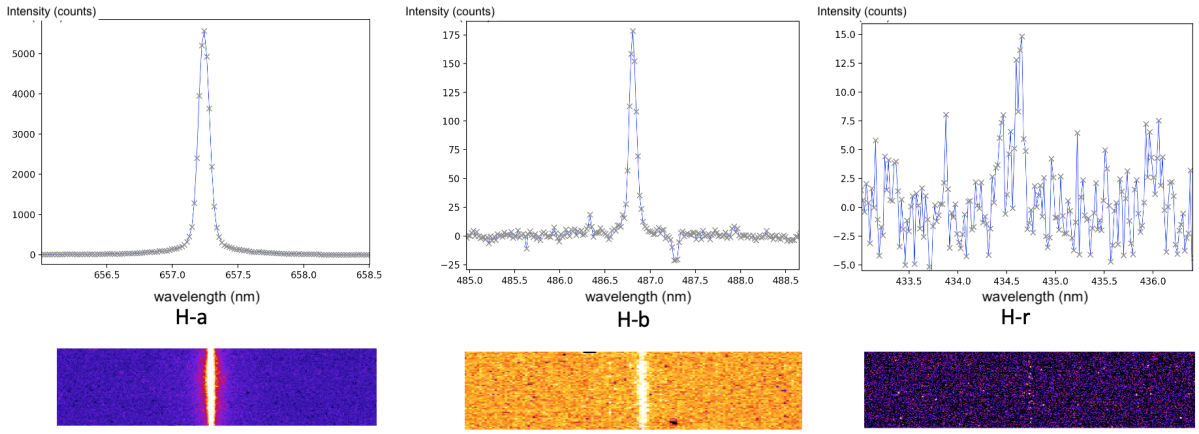

Figure 5-2: The Hydrogen Balmer (H_α, H_β and H_γ) lines in experiment. The grey crosses are the counts on the CCD. The X-axis is in nm and the Y-axis is the counts shows the intensity. Obviously the H_α line has the best S/N ratio and the H_γ has the worst.

should be a convolution with Voigt profile which gives [72, 73]

$$V = \int_{-\infty}^{+\infty} G(x, \Delta\lambda_G) L(\lambda_0 - x, \Delta\lambda_L) dx \tag{5.1}$$

As the Instrumental broadening is already known by the diagnostic resolution, in principle, first we fitting the H_β spectra and de-convolute the profile, we can get the Doppler and Stark width. This is the method to calculate the plasma electron temperature and density.

5.1.1 Estimation of plasma density by the EUV intensity

Before we apply this method to calculate the plasma parameters, it is necessary to have a roughly estimation of them. there is a scaling estimation from Horst by the EUV intensity [74],:

$$n_e = \frac{1.05\sigma_{pi} n_{gas} E_{EUV}}{A_{EUV} E_{ph}} (1 + k_{ei} n_{gas} (t_m - \frac{1}{2}\tau)) + P(E_{EUV}) - L_{fe} \tag{5.2}$$

where the factor 1.05 is average number of electrons generated per absorbed photon, σ_{pi} is the EUV / H_2 cross section (for 92 eV EUV light is $6 \times 10^{-24} m^2$), n_{gas} is the background gas pressure density, A_{EUV} is the EUV focus area, I_0 is the EUV

Intensity, τ is the duration time (10 ns), E_{ph} is the EUV photon energy (92 eV) k_{ei} is the electron impact ionization rate ($\approx 10^{-16} m^3 s^{-1}$ for several eV) t_m is the maximum n_e timing, $E_{EUV} = I_0 \tau A_{EUV}$ is the EUV energy, $P(E_{EUV})$ is the loss of pressure independent source and L_{fe} is the loss of high energy electrons. $P(EUV)$ and L_{fe} are two constant terms, $1.8 \times 10^{13} m^{-3}$ which are both ignorable in our cases.

Then we take our experimental parameters into the equation, as an example 5 Pa hydrogen gas (where the number density is $10^9 cm^{-3}$), $I_0 = 10^9 W cm - 3$, $\tau = 10 ns$ and $A_{EUV} = 150 \mu m$, The Eq.5.2 become

$$n_e = \frac{1.05 \sigma_{pi} n_{gas} I_0 \tau}{E_{ph}} = 5.65 \times 10^{13} cm^{-3} \tag{5.3}$$

This is the n_e estimation by the EUV intensity.

5.1.2 Key plasma parameter measurement by the line profile

According to the discussion above, probably, the EUV-induce hydrogen plasma in our experiment is relative low density and NLTE. It means that the methods we can use from the spectrum are limited. Another thing we must take careful is that the key parameters, T_e and n_e which are derived from line profile width also has its limitation.

There are several theoretical works which are examined widely in lots of researches before. These theories range from the model of quasi-instantaneous electron collisions of Lorentz (or impact model) [75], via the quasi-static theories for ion collisions by Kepple and Greim (KG) [69], to finally reach the recent micro-field model methods (MMM) [76]. The different theories provide expressions to calculate the Stark broadening as a function of the electron density and temperature. Except Kepple and Greim, another classical example is the theories of Vidal, Copper and Smith (VCS) [77]. One of the most refined Stark broadening theories was developed by Gigosos and Cardenoso (GC) using computer simulations [78]. The main advantage of the GC model is the consideration of ion dynamics and the possibility of working with two temperature plasmas. For these reasons the computer simulations of GC have been chosen as the Stark broadening model for the diagnostics of the electron

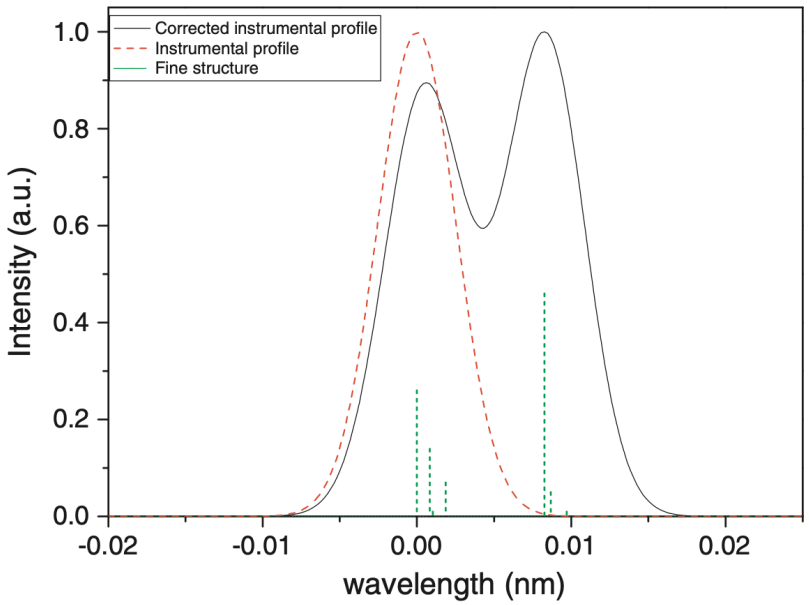

Figure 5-3: An example of H_β fine structure convolute with instrumental profile. Excepting all the broadening effect and considering the fine structure only, the spectrum are shown as the green dotted line. Assuming an instrumental profile with Gaussian profile (red dotted line), the convolution profile is the solid black line. The experimental results are the convolution of fine structure and all the broadening effects, and these effects are influenced by the plasma and diagnostic parameters.

density in this work. However, it must be said that all the mentioned theories are derived for n_e values above $10^{14} cm^{-3}$. Below this density there is no theoretical prediction with the width to density. These models limit the range because in the lower density the fine structure affect on the line profile and makes it getting far away from the standard Voigt profile.

Here we give an example of H_β to explain how the fine structure affect on the line profiles [79]. As shown in Fig.$5-3$, considering an extreme condition where the density is very low and no broadening on the spectrum, Spectra of H_β should be consisted by several separate lines. when there is a broadening mechanism exists, such as instrumental, Doppler and Stark broadening, the spectra profile should be a convolution of all the effective mechanisms. In our cases, when the plasma electron density increases and the width grows, the effect of fine structure will decrease and getting close to the Voigt profile.

This is also the reason why the theoretical predictions mentions pervious has limited to the lower boundary of $10^{14}cm^{-3}$ where the calculated n_e error is acceptable. The plasma density in our experiments may be just below this boundary, makes the situation become complex. For the plasma above this limitation, one can simply fit the spectra and de-convolute the profile and get T_e and n_e at the same time as discussed in the section 3.3.1 and 3.3.2. According to our plasma conditions, this method can lead to big errors about 50% to 100%. However, for the plasma electron density ranges between $10^{12}cm^{-3}$ and $10^{1}4cm^{-3}$, there is still a possibility to use the $\Delta\lambda_D \sim \sqrt{T_e}$ and $\Delta\lambda_S \sim \sqrt{n_e^{2/3}}$ relations That requires one of the parameters is already known. For example, if one already confirmed T_e then one can calculated a Doppler broadening width. Assuming this width contribute to Gaussian part (of course instrumental profile is considered as well) of the Voigt profile, and regard the remain width is Lorentzian which is contribute by the Stark broadening, It is still to estimate the electron density with $n_e \sim \sqrt{\Delta\lambda_S^3}$ with an error less than 20% [79].

In the experiments, H_α line has the best signal / noise ratio. As the H_α line is more sensitive to Doppler broadening, here we using a mixed method to calculate T_e and n_e.

1. Firstly, we de-convolute the H_α line and get the $\Delta\lambda_D$, and use the $T_e \sim \Delta\lambda_D$ relation to get a temperature.

2. Secondly, using the T_e to calculate a Doppler broadening width of H_β and convolute it with the instrumental broadening, then we have a Gaussian profile ($\Delta\lambda_G = \sqrt{\Delta\lambda_D^2 + \Delta\lambda_I^2}$).

3. Lastly, assuming the remain width in the H_β Voigt profile is due to the Stark broadening, and calculate the $n_e \sim \sqrt{\Delta\lambda_S^2}$.

Following the steps, we can use ORIGIN software to deal with the spectrum of H_α and H_β (Fig.5$-$4) [80]. The typical hydrogen gas pressure we used in the experiments is 5 Pa, Which is considered both for the emission observing intensity and the pressure dynamic equilibrium in the gas cell. The measurement results is shown in Tab.5.1.

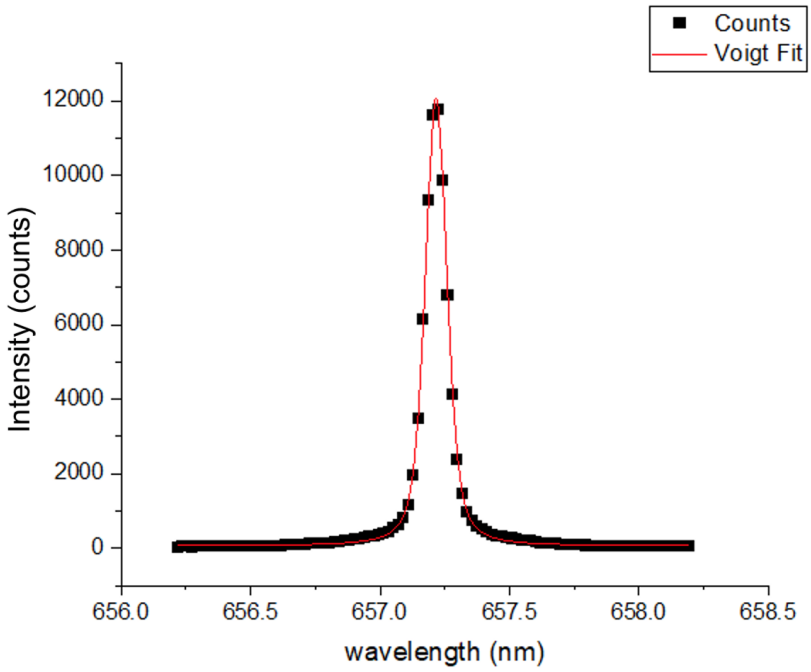

Figure 5-4: The ORIGIN software window, which fits H_α line with Voigt profile and gives the $\Delta\lambda$. Using the deconvolution method is possible to get the Lorentzian width and Gaussian width.

The first column is the background pressure in the gas cell, the second column is the plasma electron temperature derived by the H_α line profile, and the last column is the plasma electron density derived by H_β according to the steps above.

Table 5.1: Plasma T_e and n_e in the different background pressure

Pressure	$T_e(H_\alpha)$	$n_e(H_\beta)$
1.0 Pa	0.88 eV	$3.85 \times 10^{13} cm^{-3}$
2.5 Pa	1.05 eV	$4.82 \times 10^{13} cm^{-3}$
5.0 Pa	1.15 eV	$3.21 \times 10^{13} cm^{-3}$
7.5 Pa	1.21 eV	$5.32 \times 10^{13} cm^{-3}$
10.0 Pa	1.25 eV	$4.04 \times 10^{13} cm^{-3}$

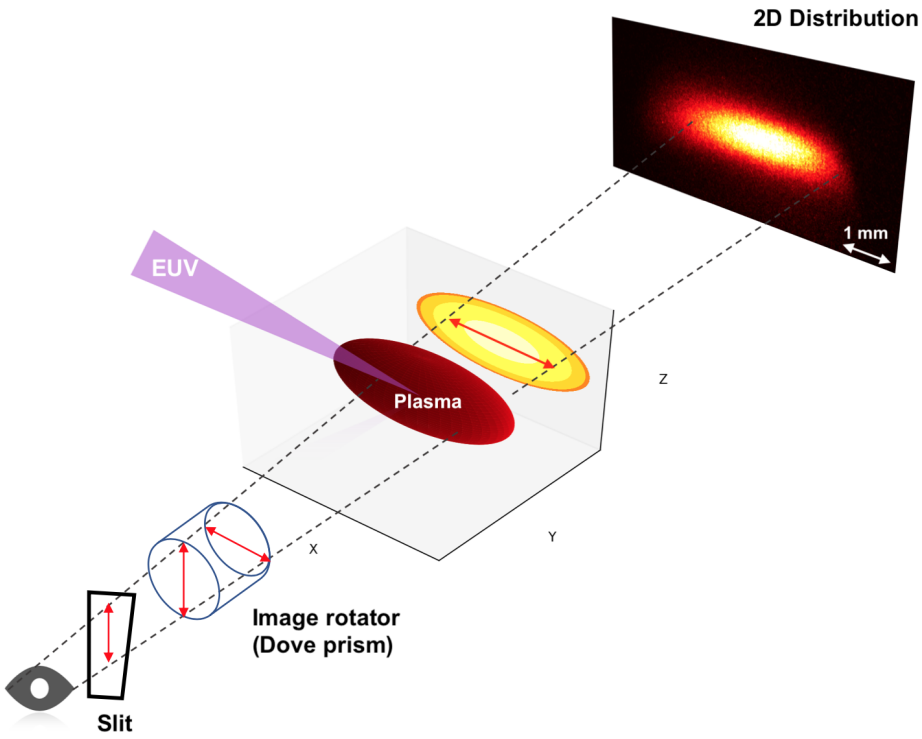

Figure 5-5: The Schematic diagram of plasma 2D distribution observation. The slit of the spectrometer limits the vision of view. In order to observe the 2D image of plasma, we fully open the slit and set up an image rotator (Dove prism) in the optical systems. It makes it possible to get the full-size image of the hydrogen plasma. By setting the different central wavelengths of the spectrometer, H_α and H_β emission image are obtained.

5.1.3 Plasma electron temperature estimation by expansion speed

The plasma electron density is already estimated by two methods, the EUV interaction rate and the line profile broadening. For plasma temperature except the line profile method we also examine it by the plasma expansion speed. In order to get the emission form the plasma by OES, we open the slit of the spectrometer and setting the central wavelength of the 1200l/mm grating to be 656 nm and 486 nm, which means that both H_α and H_β emission image are observed in the experiment. The Schematic diagram of plasma 2D distribution observing method is shown in Fig.$5-5$ The exposure time of the CCD camera is set to 10 ns, starting with 5 ns and keep the 10 ns step we get the time evolution data of the EUV-induce hydrogen plasma. The 5 Pa experimental results of H_α is shown in Fig.$5-6$ and H_β is shown in Fig.$5-7$.

As the CCD pixel size (13μm) and the OES magnification (1:1) are known, it is possible to calculate the plasma width and the expansion speed. Here we considered the horizontal FWHM as the plasma width, The plasma radius expansion with time is shown in Fig.$5-9$. The expansion radius can be perfect fit with a linear function, which indicate a constant speed of 1.12×10^6 cm/s (H_α) or 1.27×10^6 cm/s (H_β), respectively.

For hydrogen plasma the plasma sound speed (c_s) gives

$$c_s = 9.79 \times 10^5 \sqrt{\gamma T_e} \tag{5.4}$$

where γ is the adiabatic index. As the previous discussion indicate that T_e is around 1 eV, then we can get $c_s = 1.20 \times 10^6$ cm/s which has a good agreement with the observation result. It also shows that the plasma state is in a free expansion.

So far the T_e and n_e are both estimated by 2 different methods, above all here we can give a conclusion to the measurement as $T_e = 1(\pm0.2)$ eV and $n_e = 3(\pm2) \times 10^{13}$ cm^{-3}.

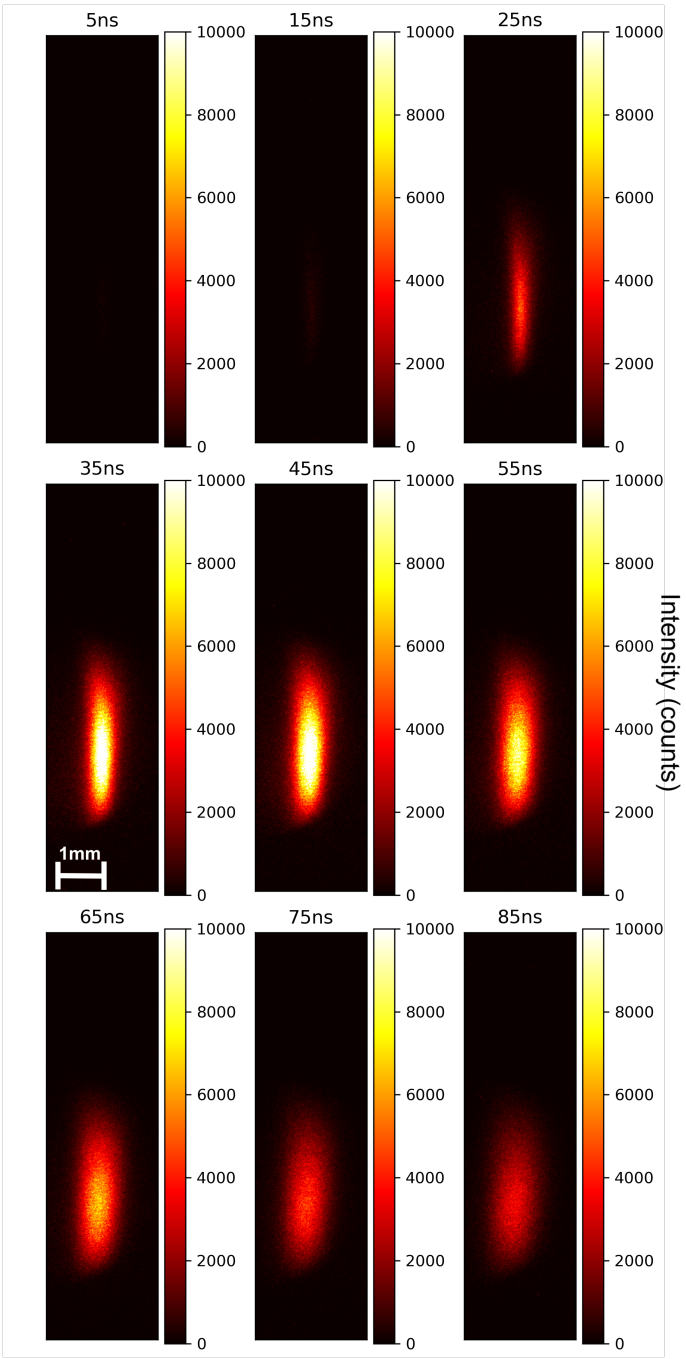

Figure 5-6: The plasma H_α image with time evolution from 5 ns to 85 ns. The plasma emission is getting stronger before 40 ns, and after that timing is getting weaker with the plasma expansion.

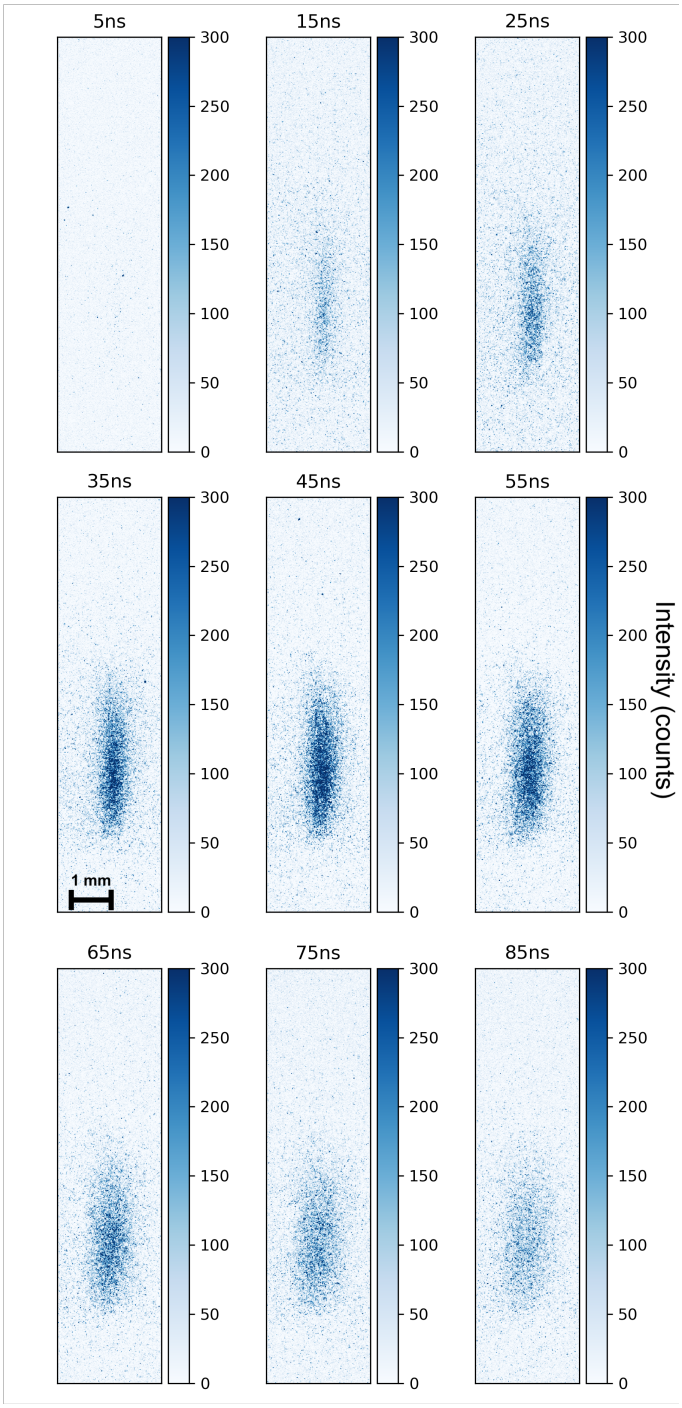

Figure 5-7: The plasma H_β image with time evolution from 5 ns to 85 ns. The similar time evolution emission of H_α are observed.

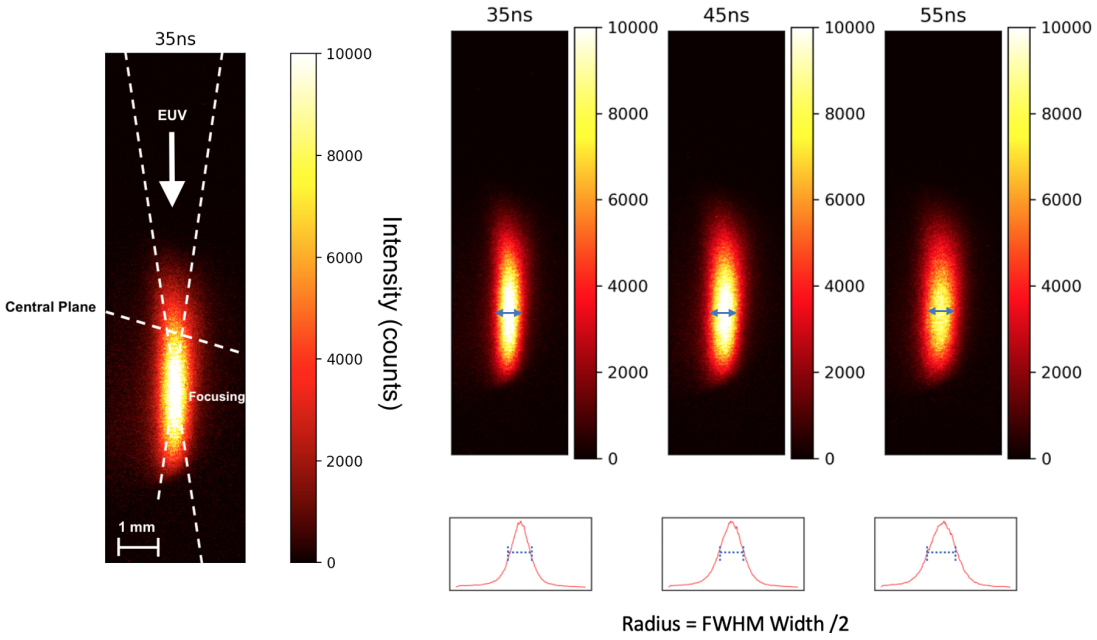

Figure 5-8: The plasma expansion speed measurement. The H_α color distribution shows the emission intensity (counts). The left pattern shows the EUV direction and the central plane, which has a 15 degree angle between them due to the Au-coated EUV mirror (see section 2.1.2). the 3 pattern in the right side show 35 ns to 55 ns emission, by measuring the horizontal distribution at the most intensive position, gives the estimation of plasma width.

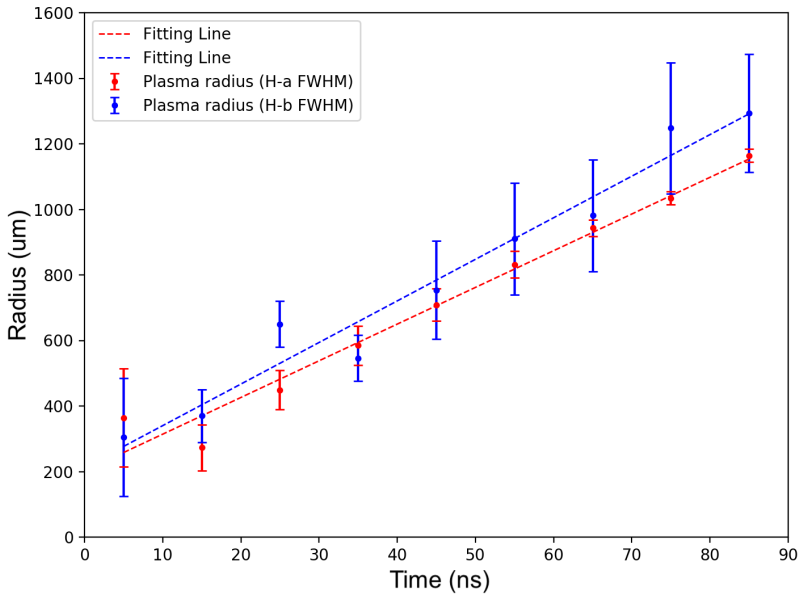

Figure 5-9: The plasma radius increasing with time. The red points are the H_α data and the blue ones are H_β data. The dotted line are the linear fitting with the least-square method. Both of H_α and H_β data show an expansion speed about 1×10^6 cm/s.

5.2 The H* population in the EUV-induced hydrogen plasma

To apply this project into the industrial application, it is necessary to promote the H* yield to $\geq 10^{15}$ cm^{-3}. This yield is an estimation which can clean the Sn drops effectively. When the EUV photons irradiate on the hydrogen gas, there are three reactions occur [16]: single photoionization (Eq.5.5), dissociative photoionization (Eq.5.6) and double photoionization (Eq.5.7).

$$\gamma + H_2 \rightarrow e^- + H_2^+(X) \tag{5.5}$$

$$\gamma + H_2 \rightarrow e^- + H_2^{+*} \rightarrow e^- + H^* + H^+ \tag{5.6}$$

$$\gamma + H_2 \rightarrow 2e^- + H_2^{2+} \rightarrow 2e^- + 2H^+ \tag{5.7}$$

where X denotes the ground state. These three reactions do not contribute to the ionization events equality which depends on the EUV photon energy. In our case, the fist one contributes to about 80%, the second one to about 15% and the third one to about 5% [81].

5.2.1 Plasma quasi steady state solution

As the H* is the only production of the bound state in the EUV / hydrogen interaction, For the purpose of estimating the H* population, we follow the steps as:

1. Building a data base of the population information of bound-state electrons in the different T_e and n_e plasmas.

2. Observing the Balmer series in the experiment (H_α, H_β, H_γ, ...), and calculating the population on each energy level.

3. Comparing the theoretical data and the experimental one, providing an estimation of H* yield based on the T_e, n_e and Balmer series data in the experiment.

In this subsection we discuss the first item, about the theoretical works. The experiment measurement will be introduced in the next subsection. A common method is calculating the population of the excited levels with the principal quantum number (p) of the quasi steady state plasma. Considering the rate equation gives

$$\begin{aligned}\frac{d}{dt}n(p) =& \sum_{q<p} C(p,q)n_e n(q) - \{[\sum_{q<p} F(p,q) + \sum_{q>p} C(p,q) + S(p)]n_e + \sum_{q<p} A(p,q)\}n(p) \\ &+ \sum_{q<p}[F(q,p)n_e + A(q,p)]n(q) + [\alpha(p)n_e + \beta(p)]n_e n_z\end{aligned} \tag{5.8}$$

where these parameters

- $n(p)$ are $n(q)$ are the population of two different excited state p, q separately.
- n_e, $n_i(= n_z)$ are number of the electrons and ions respectively, where for hydrogen we have $z = 1$.
- $C(q,p)$ is the collisional excitation from the principal quantum state of q to p.
- $F(q,p)$ is the collisional decay form q to p.
- $A(q,p)$ is the spontaneous radiation from q to p.
- $S(p)$ is the electron impact ionization from the state p.
- $\alpha(p)$ is the three-body recombination to the state p.
- $\beta(p)$ is the radiative recombination to p.

Obviously there are several processing in the CR plasmas, basically the two main process affect on the population which gives

$$n(p) = R_0(p)n_e n_i + R_1(p)n_e n(1) \tag{5.9}$$

where the first item on the right side is recombining and the second one is ionizing from the ground state atoms which including the process above by the matrix manipulation [82–84]. For hydrogen plasma here we assume $n_e = n_i$, and $n(1)$ is the background

population, in our case it related to the gas pressure which is pumped into the gas cell. For different state p here we use the modeling code by Goto.

5.2.2 The absolute population measurement of Balmer series

For the purpose of measuring the hydrogen radical (H*) yield, there are several diagnostic parameters need to be determined. Obviously, the 3 equations above indicate the spectrum of hydrogen Balmer series are only contributed by H*. As the previous description, The bound electron transition of H* is directly related to the absolute number of EUV photons which can be measured by the OES system. That provide a feasibility of calculate the hydrogen radical yield. In order to know the absolute photon number, the energy efficiency of all the opticals in the OES system including lenses, mirrors and the window of chamber flange need to be measured. These values are measured with HeNe laser (633 nm) for H_α, Cyan laser (487 nm) for H_β and H_γ separately. Besides, the solid angle of the OES system also needs to be confirmed. Based on the system design it is decided by lens 1 (Fig.2-6).

According to Fig 2-7, here we give a simple explanation of the population by the absolute intensity.

1. Observing an intensity on the CCD of H_α, H_β..., some technical parameters should be take care such as the exposure time, accumulation, etc.

2. As the system efficiency, or the response of the diagnostics and the optical solid angle are known, the photon number from the plasma can be calculated.

3. The spectrometer slit is aiming at the most intensive emission from the plasma and the actual intensity distribution may be not uniform. So the population density is characteristic and the population is related to the plasma volume assumption.

According to the discussion the plasma population can be written as

$$N(p) = F \cdot \frac{\Omega}{4\pi} \cdot t \cdot A \cdot V \cdot n(p) \tag{5.10}$$

where $N(p)$ is the photon number of principle quantum number of p, F is the system efficiency, Ω is the solid angle which is decided by the first lens, t is the exposure time, A is the Einstein coefficient and V is the plasma volume. The errors of population measurement may come from the efficiency calibration and the CCD counting fluctuations. Here we give an error value for H_α is 3%, H_β is 17.7% and H_γ is 85.8%.

5.3 H* population and cleaning rate estimation

Considering all the pervious discussion on this project, we tried to find suitable plasma parameters T_e and n_e for Goto's code modeling [85, 86]. On the other hand, the population simulated results should be comparable with the experimental ones. Under our experimental conditions, only H_α ($n(3)$), H_β $n(4)$and H_γ ($n(5)$) spectrum are observed. The results comparison are shown in Fig.$5-10$. The difference between two pattern is the exposure timing, the left one is 0-50 ns exposure and the right one is 20-60 ns. Three electron density states are chosen, 1.0×10^{19} cm-3, and 5.0×10^{19} cm-3 which are in red and blue separately. the dotted line is the population which not only considers the recombination process ($R_0(p)n_e^2$) but also the ionization, which gives the total population ($n(p)$). The experimental results are shown in black dotted line. The temperature are set to 1.1 eV for the best fitting. The X-axis are the principle quantum number and the Y-axis are population in m^{-3}.

The black dots are the experimental data of H_α ($n(3)$), H_β $n(4)$and H_γ ($n(5)$) absolute population by directly measurement. Here we can see that there is a good agreement of the first three Balmer series population density in this plasma parameters. There are some disagreement in H_α ($n(3)$), a possible reason is that the modeling does not including all the physical processes in the photon-ionization process. But for H_β $n(4)$and H_γ ($n(5)$) the results are satisfied for the estimation of population. Although other Balmer lines are invisible under our experimental conditions, according to the similarity between the measurement results and the modeling ones, we can combine the experiment data n(3-5), assume a Boltzmann distribution to estimate n(1), provide n(2) and n(6-10) by modeling, then the population of first 5 levels

Table 5.2: n(p) populations of (0-50 ns average)

n(p)	population density	method
n(1)	3.6×10^{12} cm^{-3}	calculation
n(2)	3.7×10^{8} cm^{-3}	modeling
n(3)	1.7×10^{8} cm^{-3}	experiment
n(4)	1.6×10^{7} cm^{-3}	experiment
n(5)	6.0×10^{6} cm^{-3}	experiment

are shown in Tab.5.2. it is possible give an estimation of the H* population density according to the discussion above:

$$\sum_{n=1}^{10} n(p) = 3.7 \times 10^{12} cm^{-3} \tag{5.11}$$

The error is estimate as ≤ 1 order, This value is still much smaller than the typical cleaning density which are aimed at in the beginning. In future the industrial application experiment, the Sn cleaning and the cleaning efficiency will be tested. That will give the information about this condition.

Based on the H* population result, the author estimate the cleaning effect of value 3.7×10^{12} cm^{-3}. First we assume a Sn cube on the sample surface (Fig.5-11). The Sn number density is known as 3.7×10^{22} cm^{-3}, then we think about a mono-layer Sn, which gives a density of $n_{mono} = (3.7 \times 10^{22} cm^{-3})^{2/3} = 1.1 \times 10^{15} cm^{-2}$.

According to the CRC handbook the Sn mono-layer average thickness is 0.434 nm [87]. Considering the H* population results mention above and the cleaning rate can be calculated with

$$R_c = \frac{n(H*) \cdot 6300 \cdot 0.434}{4 \times n_{mono}} \tag{5.12}$$

where the factor of 6300 means there are 6300 shots per experiments and the factor of 4 because of Sn+4H*$\rightarrow$SnH$_4$ reaction. In this conditions the estimating results of Sn cleaning rate is 2.18 nm/exp.. This value means that in there are about 2.18 nm thickness of Sn is cleaned per unit area (cm^2) per experiment.

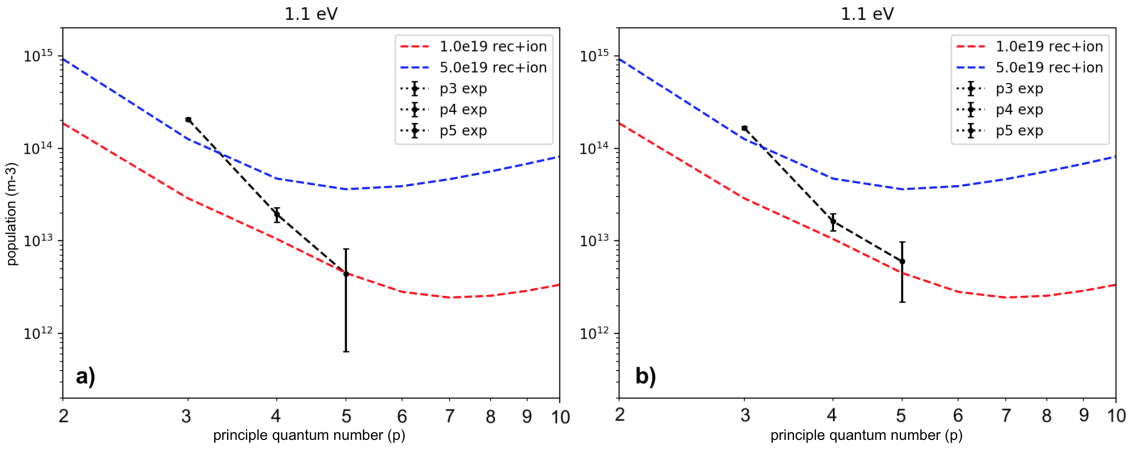

Figure 5-10: The comparison of modeling and experiment $n(p)$ of 1.1 eV temperature. a) 0-50 ns and b) 20-60 ns average population of 5 Pa gas cell pressure. The X-axis is the principle quantum number (p) and the Y-axis is the population in the unit of m^{-3}. The red dotted line is the $n_e = 1 \times 10^{13} cm^{-3}$ and The blue one is $n_e = 5 \times 10^{13} cm^{-3}$, and the black dotted line shows the experimental data. Both ionization and recombination which contribute to the population are considered. It can be seen that the experiment results lay in the theoretical estimate region. For H_α (p=3) population there are some deviation between the modeling and experiment one.

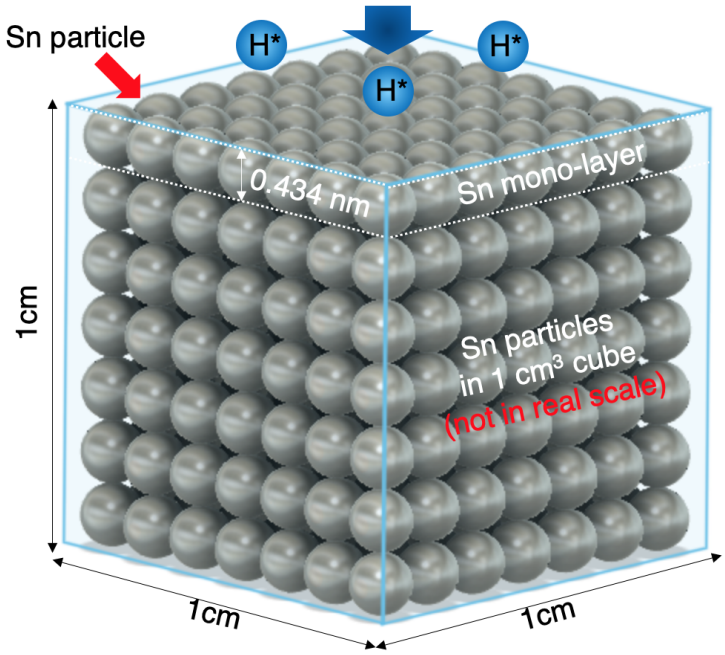

Figure 5-11: The diagrammatic of Sn sample surface. The H* will contact the surface top and the reaction happens.

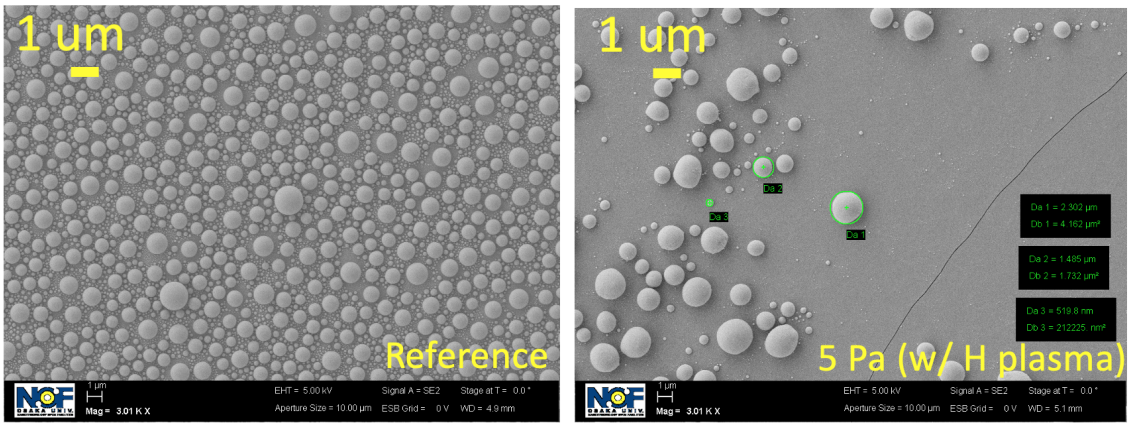

Figure 5-12: The experimental result of Sn cleaning. The left pattern is the reference with out hydrogen in the gas cell, and the right one is the with hydrogen plasma result. Obviously there is a cleaning effect exists. The patterns are obtained by the SEM.

5.4 Sn cleaning experiment

For the propose of examining the Sn cleaning result, a Sn cleaning experiment are also performed. In this experiment the author also used 5 Pa Hydrogen gas for plasma generation, and put a small Sn sample in the central plane of the gas cell. The experimental results are analyzed by the scanning electron microscope (SEM).

The SEM results are shown in Fig.5-12. According to the reference results, here the author assumes that each Sn particulates is sphere. This is a reasonable assumption according to the sample side-view SEM images as well. As the real radius of the particulate can be measured by the scaling, one can calculate a total volume V_{Sn} of the Sn in the view by counting all the particulates in the view and the statistics of particulate diameter distribution. The total size of view is known as S_{sem}, The cleaning rate can be measured as

$$R_c = \frac{\Delta V_{Sn}}{S_{sem}} \tag{5.13}$$

where the ΔV_{Sn} is the cleaned Sn volume. The SEM analyzation gives $R_c = 75.6$ nm/exp..

5.5 Summary of EUV project for H* measurement and atomic process

In the EUV-induced hydrogen plasma research, the author built a good accessibility and compact EUV source and OES system for laboratory experiment. The author measured the high intensity EUV-induced hydrogen plasma parameters, and estimate the Sn cleaning rate of H*. Finally the author compared the cleaning rate from the theoretical estimation and the SEM analyzation. The detailed achievements are:

1. The author builds an OES system which can be used not only for the spectroscopy but also the 2D emission measurement. The spectra profile can be used for calculation the $T_e \approx 1.1$ eV and $n_e \approx 2 \times 10^{13}$ cm^{-3}. The 2D emission provides another method to confirm these plasma parameters.

2. The absolute photon numbers and the H_α, H_β and H_γ were used to calculated the H* populations. By using Dr.Goto's code, the total H* population was calculated as 3.7×10^{12} cm^{-3}.

3. According to the H* population the cleaning rate was estimated and comparing with the SEM measurement results.

As shown in Fig.5-13 there is a best fitting of the plasma parameter, but there is still a small disagreement in the H_α populations. Indicating that the population of excited atoms can not be explained only by quasi-steady modeling. As the spectrum S/N ratio is relative low for the high time resolution measurement, The 2D emission of the H_α and H_β are also measured. The time evolution of intensity changes are in Fig.5-14.

In the first 40 ns the intensity ratio of H_α and H_β is not stable, indicating that the plasma is not the quasi-steady state. the hot electrons (which are directly ionized by the 100 eV EUV) may play a role in this process. After 40 ns the two lines goes smoothly and ratio become steady, indicating the plasma comes into the equilibrium.

The Fig.5-10 also indicating this possibility. As the EUV irradiation is in 0-10 ns with Gaussian profile, comparing the two time average experiment results 0-50ns

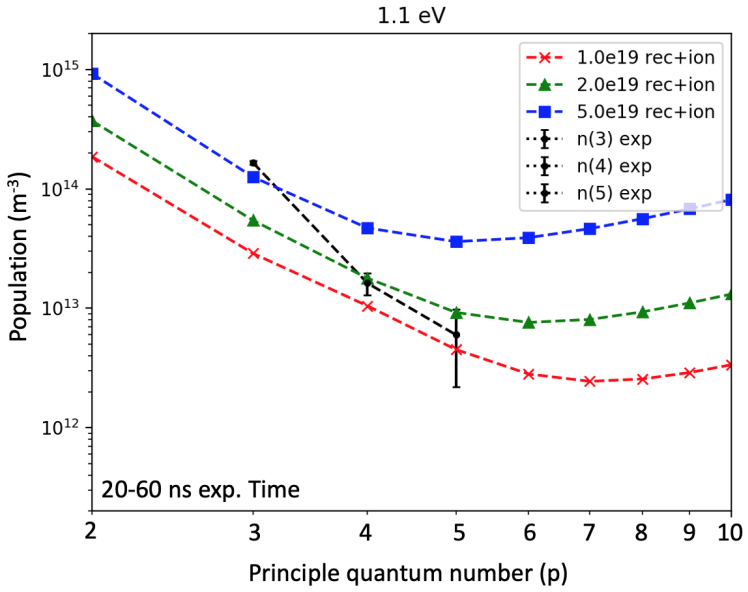

Figure 5-13: The best fitting of the experiment result form the exposure time 20-60 ns, gives a average $T_e \approx 1.1$ eV and $n_e \approx 2 \times 10^{13}$ cm^{-3}.

and 20-60 ns the latter one gives better population fitting. Because the 0-50 ns result includes the EUV duration time and 20-60 the effect of the EUV is getting weaker.

Another thing worthy to talk about in Fig.5-10 and Fig.5-13 is that the H_β and H_γ population are seem fitting better in 20-60 ns as well. But the effects are not as significant as H_α. There is a possibility that the fast electrons affect on all the energy levels but the time scale are different with each other. As the experiment begins, some fast electrons are ionized directly by the EUV with about 100 eV energy, and after about 40 ns collision and interaction, the plasma cooling down and become equilibrium with 1 eV temperature. To confirm this idea, a possible way is to use high sensitive diagnostics which can observe the H_γ emissions with time evolution. And observing the average T_e and n_e after 40 ns to confirm the existence of quasi-steady state.

From the comparison of the theoretical estimated rate and the SEM analyzed one, obviously the cleaning rate of hydrogen plasma was underestimate if as some pervious researches simply ascribing the clean effect only due to H*. The experimental measurement shows that there are other effects contribute to the Sn particles cleaning. The EUV directly evaporation may be a possible reason, and may be some other un-

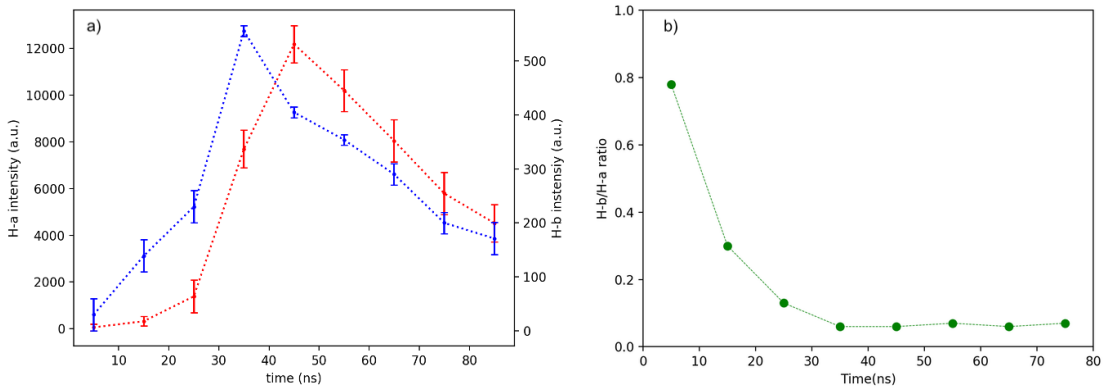

Figure 5-14: a). The H_α and H_β intensity time evolution from the 2D emission image. The EUV irradiation is in 0-10 ns with Gaussian profile. b). The emission ratio time changes of H_β/H_α. It can be seen that the intensity ratio became constant after about 40 ns.

known fractions in the plasma react with Sn. In order to do such an analyzation there is a method to couple a retarding field energy analyzers (RFEAs) and electrostatic quadrupole plasma (EQP) to get the detailed plasma particle fractions.

Chapter 6

Conclusion

In the thesis, the author introduces two applications of spectroscopy science which are EUV related. The first project is a numerical modeling and design for observing the EUV bandwidth Zeeman splitting in laser-produce magnetized plasma. In the modeling a low density (10^{21} cm^{-3}) Si plasma is generated in a 10 kT level magnetic field. The plasma temperature is about 100 eV. The author confirmed the plasma parameters with MHD method and calculate an observable splitting at 96 eV Si VII line, which provides a guidance for the present and future high-field Zeeman splitting experiment. The second project is using the frost Xe target to generate a 12 nm EUV light source. The EUV are focused and induced into the Hydrogen gas cell, to generate the high intensity EUV-induced hydrogen plasma. Then detecting the EUV-induced hydrogen plasma parameters which is not well researched in the plasma physics, and determine the possibility of applying H* for the Sn particle cleaning.

The Zeeman splitting experiment plan is aiming at the basic science researches. The primary goal is to confirm the existence of the magnetic field by the Zeeman effect. Another goal of this project is if the field strength is high enough which the non-linear Zeeman effect may occur, it is possible to compare this result to the astronomical observation in the magnetars. In the experiment trials we observed some potential effects of Zeeman splitting, but to confirm the result some further experiment and additional diagnostics are needed, such as the self-emission diagnostics for checking the plasma compression, and proton back-lighter target for magnetic field generation

cross-check. These will help us to promote the success rate.

The EUV-induce hydrogen plasma experiment also has the important meaning for the basic science, where the EUV-induce plasma is a not-well-researched region in the plasma physics. This research may contribute to this topic, especially the plasma key parameters, the plasma electron temperature and density. The other exciting possibility is that one of the EUV-induce hydrogen plasma productions, The H* may clean the Sn ions in the reaction chamber and if we successfully apply this technology it may promote the efficiency in EUVL applications. According to our experiment results, there is a significant cleaning rate in the SEM analyzation (75.6 nm/exp.), which is much higher than the theoretical estimation rate (2.18 nm/exp.). The result proves the feasibility of applying the H* to Sn cleaning in EUVL. But it also indicates that some pervious researches claim the effect is only caused by H* may be not exactly correct. The H* is not the only factor in the cleaning effects. The EUV irradiation and the other plasma fractions may also have cleaning effects.

In the future, it is still possible to improve the Zeeman splitting experiment design and diagnostics, then applicate it into the experiment on big facilities, including but not limit to the Gekko-LFEX system. About the EUV-induce plasma project, as we developed a method to calculate the key plasma parameters, it will promote our understanding of EUV-induced plasma, and partly explain the Sn particle cleaning effect in the EUVL.

Appendix A

OES efficiency measurement

The quantum efficiency (QE) of the OES system is one of the important parameters for the absolute photon number calculation. It is a ratio which is defined as the incident photon to converted electron (IPCE) ratio:

$$QE = \frac{electrons/sec}{photons/sec} \tag{A.1}$$

The system efficiency in Eq.5.10 is represented as the factor F, for the OES system in this research, F includes two parts: the optical systems efficiency and the QE of the spectrometer & ICCD system.

A.1 The efficiency of optical system

In order to measure the efficiency, a simple idea is using a photodiode to measure the emission ability of a light source, for example, a laser device. And comparing the emission ability after the opticals which are need to measure the efficiency. The ratio can be the optical efficiency. The method is shown in Fig.A-1.

For the population measurement of hydrogen Balmer series, obviously the light source wavelength should be similar to the specific spectra as much as possible. Considering about the limitation of the light source, two kind of laser is used for measuring. HeNe laser (633 nm) and L488P60 laser (488 nm) are used to measure the

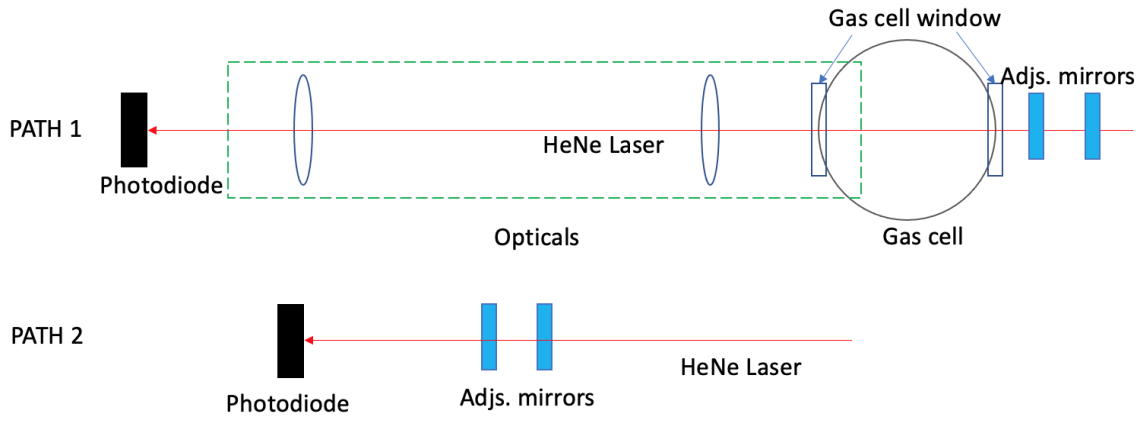

Figure A-1: The method to calculate the efficiency optical system. In the path 1, the laser source goes through all the opticals while in path 2 is not. The photodiode is connect to an oscilloscope, by comparing the voltage ratio between path 1 & 2 it is possible to get the system efficiency.

H_α (656 nm) and H_β (486 nm), respectively. The measurement results give the H_α efficiency of 19%, and give H_β efficiency of 17.2%. As there is no suitable laser source for H_γ (434 nm), in this research we use the H_β efficiency to instead.

One thing needs to be noticed is that the error in the measurement, as the wavelengths are not 100% same to the H_α and H_β, also the H_γ there is about 50 nm difference to the "standard" laser. The errors are taking into account in the population calculation results, see section 5.3.

A.2 The efficiency of spectrometer & ICCD system

The QE of spectrometer & ICCD system is calibrated by HAMAMATSU L2196 D2 Deuterium lamp. Although L2196 is usually used as a UV light source, the output power in visible bandwidth is also known. The power output is shown as Fig.A-2. Hence, we set the lamp 50 cm from the spectrometer slit and measure the counts at H_α, H_β and H_γ. At the specific wavelength (λ) the total energy (E_{ph}) can be calculated as

$$E_{ph} = I \cdot t \cdot s \cdot \lambda \tag{A.2}$$

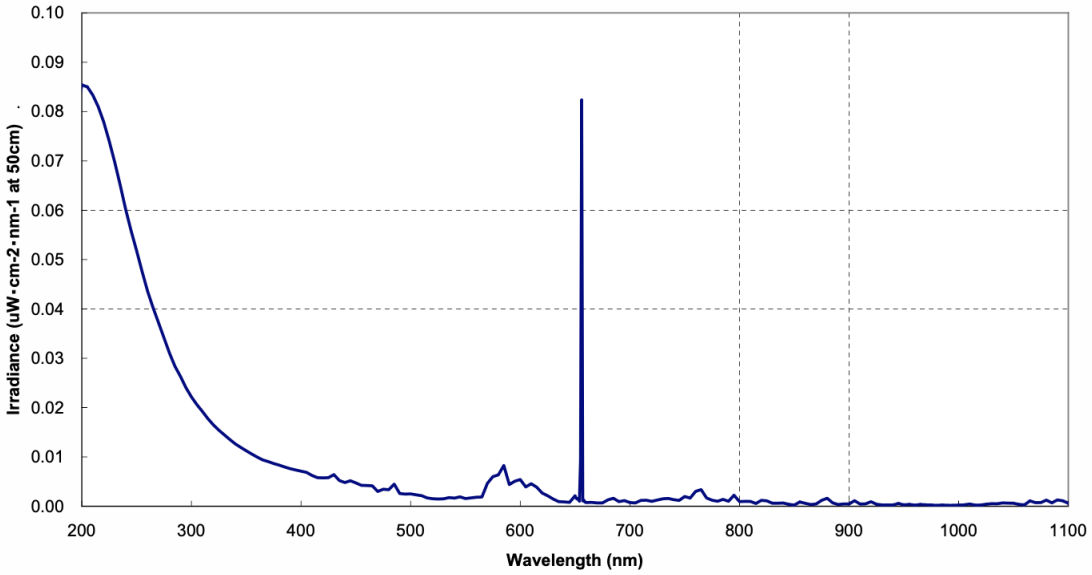

Figure A-2: The power output of Deuterium lamp. The output in visible band is lower than UV one. The X-axis is the wavelength in nm with 1 nm resolution and the Y-axis is the irradiance power with unit $uW \cdot cm^{-2} \cdot nm^{-1}$ at 50 cm distance. (Source: HAMAMATSU Corp.)

where I is the irradiance power, t is the exposure time and s is the slit size. Then the photon number can be easily calculated by E_{ph}/E_n, E_n stands for the specific photon energy of the spectra. According to the Eq.A.1, The QEs of the first three Balmer lines are 0.08, 0.12 and 0.12, respectively.

Considering all the factors above, the F is the product of the spectrometer & ICCD's QE and the optical efficiency.

Appendix B

FLASH setting up for MHD modeling in the Zeeman measurement

```
subroutine Simulation_initBlock(blockId)
  use Simulation_data
  use Grid_interface, ONLY : Grid_getBlkIndexLimits, &
       Grid_getCellCoords, Grid_putPointData,&
                           Grid_getBlkPtr,         &
                           Grid_releaseBlkPtr

  use Driver_interface, ONLY: Driver_abortFlash
  use RadTrans_interface, ONLY: RadTrans_mgdEFromT

  implicit none

#include "constants.h"
#include "Flash.h"

  ! compute the maximum length of a vector in each coordinate direction
  ! (including guardcells)

  integer, intent(in) :: blockId

  integer :: i, j, k, n
  integer :: blkLimits(2, MDIM)
  integer :: blkLimitsGC(2, MDIM)
  integer :: axis(MDIM)
  real, allocatable :: xcent(:), ycent(:), zcent(:)
  real :: tradActual
  real :: rho, tele, trad, tion, zbar, abar
  integer :: species
  real, pointer, dimension(:,:,:,:) :: facexData,faceyData
#if NDIM > 0
  real, pointer, dimension(:,:,:,:) :: facezData
#endif

#ifndef CHAM_SPEC
  integer :: CHAM_SPEC = 1, TARG_SPEC = 2, TAR2_SPEC=3, TAR3_SPEC=4,  WALL_SPEC=5
#endif
```

```
  ! get the coordinate information for the current block from the database
  call Grid_getBlkIndexLimits(blockId,blkLimits,blkLimitsGC)

  ! get the coordinate information for the current block from the database
  call Grid_getBlkIndexLimits(blockId,blkLimits,blkLimitsGC)
  allocate(xcent(blkLimitsGC(HIGH, IAXIS)))
  call Grid_getCellCoords(IAXIS, blockId, CENTER, .true., &
       xcent, blkLimitsGC(HIGH, IAXIS))
  allocate(ycent(blkLimitsGC(HIGH, JAXIS)))
  call Grid_getCellCoords(JAXIS, blockId, CENTER, .true., &
       ycent, blkLimitsGC(HIGH, JAXIS))
  allocate(zcent(blkLimitsGC(HIGH, KAXIS)))
  call Grid_getCellCoords(KAXIS, blockId, CENTER, .true., &
       zcent, blkLimitsGC(HIGH, KAXIS))

#if NFACE_VARS > 0
  if (sim_killdivb) then
     call Grid_getBlkPtr(blockID,facexData,FACEX)
     call Grid_getBlkPtr(blockID,faceyData,FACEY)
     if (NDIM>2) call Grid_getBlkPtr(blockID,facezData,FACEZ)
  endif
#endif

  !!----------------------------------------------------------------------

  ! Loop over cells and set the initial state
  do k = blkLimits(LOW,KAXIS),blkLimits(HIGH,KAXIS)
     do j = blkLimits(LOW,JAXIS),blkLimits(HIGH,JAXIS)
        do i = blkLimits(LOW,IAXIS),blkLimits(HIGH,IAXIS)

           axis(IAXIS) = i
           axis(JAXIS) = j
           axis(KAXIS) = k

           species = CHAM_SPEC
          if (sim_initGeom == "slab") then
              if(NDIM == 1) then
                 if ( xcent(i) <= sim_targetHeight + sim_vacuumHeight .and. &
                      xcent(i) >= sim_vacuumHeight ) then
                    species = TARG_SPEC
                 end if

              elseif(NDIM == 2 .or. NDIM == 3) then

                if ( ABS(xcent(i)) <= sim_walloutRadius .and. &  !!added for wall
                     ABS(xcent(i)) >= sim_wallinRadius .and. &
                     ycent(j) <= sim_wallYmax .and. &
                     ycent(j) >= sim_wallYmin ) then
                     species = WALL_SPEC
                end if
                if ( (ABS(xcent(i)) <= sim_targetRadius) .and. &
                      ycent(j) <= sim_targetYmax .and. &
                      ycent(j) >= sim_targetYmin ) then
                   species = TARG_SPEC
                  ! write(*,*)"foam"
                end if
                if (  ABS(xcent(i)) <= sim_target2Radius .and. &
                          (ycent(j)>=sim_target2Ymin .and. &
                            ycent(j)<sim_wallYmin)) then
                       species = TAR2_SPEC
```

```
            !write(*,*) "cone bottom"
      end if
      if (  ABS(xcent(i)) <= sim_target3Radius .and. &
                  (ycent(j)<sim_target3Ymax .and. &
                  ycent(j)>sim_wallYmax)) then
                    species = TAR3_SPEC
      end if
          !    write(*,*) "cone top"
      if( ABS(ycent(j)) > sim_wallYmax .and. &
                 ABS(ycent(j))>(sim_target2a1*ABS(xcent(i))+sim_target2b1) .and. &
                 ABS(ycent(j))<(sim_target2a1*ABS(xcent(i))+sim_target2b2))then
            !       write(*,*) "cone"

                !! the sentence below is for cylinder cover
                !!ABS(xcent(i)) > sim_target2inRadius) .and. &
                !!   (  (ycent(j)<=sim_target2outYmax .and. &
                !!     ycent(j)>sim_wallYmax ) .or. &
                !!    (ycent(j)>=sim_target2outYmin .and. &
                !!     ycent(j)<sim_wallYmin) )) then
                !! over
                species = CONE_SPEC
      end if
   endif
else !!sphere
    if (sqrt(xcent(i)**2+ycent(j)**2+zcent(k)**2)<= sim_targetRadius) then
       species = TARG_SPEC
   end if
end if
if(species == TARG_SPEC) then
   rho = sim_rhoTarg
   tele = sim_teleTarg
   tion = sim_tionTarg
   trad = sim_tradTarg
else if(species == TAR2_SPEC) then
      rho = sim_rhoTar2
      tele = sim_teleTar2
      tion = sim_tionTar2
      trad = sim_tradTar2
     ! write(*,*) xcent(i),ycent(i),sim_target2a1*ABS(xcent(i))+sim_target2b1,i,j,k
   !   write(*,*)sim_rhoTar2
else if(species == TAR3_SPEC) then
       rho = sim_rhoTar3
       tele = sim_teleTar3
       tion = sim_tionTar3
       trad = sim_tradTar3
else if(species == CONE_SPEC) then
            rho = sim_rhoCone
            tele = sim_teleCone
            tion = sim_tionCone
            trad = sim_tradCone
else if(species==WALL_SPEC) then  !!added
   rho = sim_rhoWall
   tele = sim_teleWall
   tion = sim_tionWall
   trad = sim_tradWall
else
   rho = sim_rhoCham
   tele = sim_teleCham
   tion = sim_tionCham
   trad = sim_tradCham
```

```
            end if
           ! write(*,*) "check point 3",xcent(i),ycent(i),species, rho

            call Grid_putPointData(blockId, CENTER, DENS_VAR, EXTERIOR, axis, rho)
            call Grid_putPointData(blockId, CENTER, TEMP_VAR, EXTERIOR, axis, tele)

#ifdef FLASH_3T
            call Grid_putPointData(blockId, CENTER, TION_VAR, EXTERIOR, axis, tion)
            call Grid_putPointData(blockId, CENTER, TELE_VAR, EXTERIOR, axis, tele)

            ! Set up radiation energy density:
            call RadTrans_mgdEFromT(blockId, axis, trad, tradActual)
            call Grid_putPointData(blockId, CENTER, TRAD_VAR, EXTERIOR, axis, tradActual)
#endif
            if (NSPECIES > 0) then
               ! Fill mass fractions in solution array if we have any SPECIES defined.
               ! We put nearly all the mass into either the Xe material if XE_SPEC is defined,
               ! or else into the first species.
               do n = SPECIES_BEGIN,SPECIES_END
                  if (n==species) then
                     call Grid_putPointData(blockID, CENTER, n, EXTERIOR, axis, 1.0e0-(NSPECIES-1)*sim_smallX)
                  else
                     call Grid_putPointData(blockID, CENTER, n, EXTERIOR, axis, sim_smallX)
                  end if
               enddo
            end if

#ifdef BDRY_VAR
            call Grid_putPointData(blockId, CENTER, BDRY_VAR, EXTERIOR, axis, -1.0)
#endif


#if NFACE_VARS > 0
            !! In this case we initialized Az using the cell-cornered coordinates.
            if (sim_killdivb) then
               if (NDIM == 2) then
                  facexData(MAG_FACE_VAR,i,j,k)= 0.0
                  faceyData(MAG_FACE_VAR,i,j,k)= 0.0
                  if (NDIM>2) facezData(MAG_FACE_VAR,i,j,k)= 0.0
               endif
            endif
#endif
!end if
         enddo
      enddo
   enddo
#if NFACE_VARS > 0
   if (sim_killdivb) then
      call Grid_releaseBlkPtr(blockID,facexData,FACEX)
      call Grid_releaseBlkPtr(blockID,faceyData,FACEY)
      if (NDIM>2) call Grid_releaseBlkPtr(blockID,facezData,FACEZ)
   endif
#endif
   deallocate(xcent)
   deallocate(ycent)
   deallocate(zcent)

   return

end subroutine Simulation_initBlock
```

Appendix C

The script used for the EUV-induce plasma measurement

C.1 Plasma election temperature calculation

```
import numpy as np
from scipy import constants

print("#################################################################")
print("#
#")
print("#     This script is for Doppler Te, Please confirm before calculation!      #")
print("#
#")
print("#################################################################")
while True:
    try:
        w_g=float(input('Please input the Gaussian line broadening (nm):'))
        lambda_0=float(input("please input the center wavelength (nm):"))
        w_i=float(input('Please input the instrument resolution (nm):'))
        break
    except(IOError, SyntaxError, TypeError, NameError):
        print('Input error,try again:')

w_d=np.sqrt(np.square(w_g)-np.square(w_i))

m=1 #hydrogen

T_k=np.square(w_d/(7.16e-7*lambda_0))*m
T_e1=T_k/11605
T_e=round(T_e1,2)

print("The Te is {} eV".format(T_e))
```

C.2 Plasma electron number density calculation

```
import numpy as np
from scipy import constants
print('#####################################################################')
print('#
#')
print('# This script is for 2400g/mm H-beta! Please confirm before calculation!  #')
print('#
#')
print('#####################################################################')

while True:
    try:
        lamda=float(input('please input the line L FWHM broadening (nm):'))
        break
    except(IOError, SyntaxError, TypeError, NameError):
        print('Value error, try again:')

lamda_n=lamda*10
x=lamda_n/(7.4e-19*np.square(4861.35)*12)
ne=pow(x, 1.5)
print(ne)
if ne < 0:
    print("Error: negative density!")
else:
    print('The electron density is {:g} cm-3'.format(ne))
```

C.3 H* calculation

```
from scipy import constants

cts3=float(input("please input the H-alpha counts:"))
cts4=float(input("please input the H-beta counts:"))
cts5=float(input("please input the H-gamma counts:"))

sw=15e-4 #slit width in cm
p=13e-4 #CCD pixel size in cm
ro=0.16#0.28 #0.12 #radius of CCD observable region in cm
re=0.16 #100e-4 #radius of EUV radiation volume in cm
rl=2.415 #radius of the first lens in cm
R=30 #distance of the first lens to TCC in cm

A_slt=94*p*sw # region size chosen on CCD in cm-2
A_obs=ro**2*constants.pi # observation emission area on CCD in cm-2, R=0.12 cm
V_euv=(4*constants.pi*re**3)/3  #4.189e-6 # EUV volume in cm-3, R=0.01 cm
omega=(rl**2*constants.pi)/(R**2) # solid angle of the first lens, R=2.415 cm with d=30 cm

obs_n3=4*constants.pi*(((cts3/A_slt)*A_obs)/(900*100))/omega #H-alpha total counts
obs_n4=4*constants.pi*(((cts4/A_slt)*A_obs)/(900*100))/omega  #H-beta total counts
obs_n5=4*constants.pi*(((cts5/A_slt)*A_obs)/(900*100))/omega

t=10 #ns

n3=(obs_n3/t)/0.044123
n4=(obs_n4/t)/8.4193e-3
n5=(obs_n5/t)/2.5304e-3

```

```
29 dens=(n3+n4+n5)/V_euv
30 #print(omega)
31 print("the population of n=3 is %.3e"%(n3/V_euv))
32 print("the population of n=4 is %.3e"%(n4/V_euv))
33 print("the population of n=5 is %.3e"%(n5/V_euv))
34 print("the H* density is %.3e cm-3"%(dens))
```

Bibliography

[1] Hans R Griem. High-density corrections in plasma spectroscopy. *Physical Review*, 128(3):997, 1962.

[2] John Cooper. Plasma spectroscopy. *Reports on Progress in Physics*, 29(1):35, 1966.

[3] Hans R Griem. *Principles of plasma spectroscopy*, volume 2. Cambridge University Press, 2005.

[4] Takashi Fujimoto. Plasma spectroscopy. In *Plasma Polarization Spectroscopy*, pages 29–49. Springer, 2008.

[5] Chang Liu, Kazuki Matsuo, Sandrine Ferri, Hyun-Kyung Chung, Seungho Lee, Shohei Sakata, King Fai Farley Law, Hiroki Morita, Bradley Pollock, John Moody, et al. Design of zeeman spectroscopy experiment with magnetized silicon plasma generated in the laboratory. *High Energy Density Physics*, 33:100710, 2019.

[6] Shinsuke Fujioka, Zhe Zhang, Kazuhiro Ishihara, Keisuke Shigemori, Youichiro Hironaka, Tomoyuki Johzaki, Atsushi Sunahara, Naoji Yamamoto, Hideki Nakashima, Tsuguhiro Watanabe, Hiroyuki Shiraga, Hiroaki Nishimura, and Hiroshi Azechi. Kilotesla magnetic field due to a capacitor-coil target driven by high power laser. *Scientific Reports*, 2013.

[7] K. F.F. Law, M. Bailly-Grandvaux, A. Morace, S. Sakata, K. Matsuo, S. Kojima, S. Lee, X. Vaisseau, Y. Arikawa, A. Yogo, K. Kondo, Z. Zhang, C. Bellei, J. J.

Santos, S. Fujioka, and H. Azechi. Direct measurement of kilo-tesla level magnetic field generated with laser-driven capacitor-coil target by proton deflectometry. *Applied Physics Letters*, 108(9):1–6, 2016.

[8] G Hinshaw, N Jarosik, a Kogut, M Limon, S S Meyer, L Page, G S Tucker, J L Weiland, E Wollack, and E L Wright. The American Astronomical Society. All rights reserved. Printed in U.S.A. *Analysis*, 5:175–194, 2003.

[9] Karen M Vanlandingham, Gary D Schmidt, Daniel J Eisenstein, Hugh C Harris, Scott F Anderson, Patrick B Hall, James Liebert, Donald P Schneider, Nicole M Silvestri, Gregory S Stinson, and Michael a Wolfe. Magnetic White Dwarfs from the SDSS. II. The Second and Third Data Releases. *The Astronomical Journal*, 130:734–741, 2005.

[10] D. T. Wickramasinghe and Lilia Ferrario. The origin of the magnetic fields in white dwarfs. *Monthly Notices of the Royal Astronomical Society*, 356(4):1576–1582, 2005.

[11] Bradley W Carroll and Dale A Ostlie. *An introduction to modern astrophysics*. Cambridge University Press, 2017.

[12] Thanu Padmanabhan. *Theoretical Astrophysics: Volume 1, Astrophysical Processes*. Cambridge University Press, 2000.

[13] Hannu Karttunen, Pekka Kröger, Heikki Oja, Markku Poutanen, and Karl Johan Donner. *Fundamental astronomy*. Springer, 2016.

[14] S Laustsen, C Madsen, and RM West. Astronomy and astrophysics library.

[15] K. Croswell. *The alchemy of the heavens*. Oxford University Press, Oxford (UK), 1996.

[16] R M Van Der Horst, J Beckers, E A Osorio, D I Astakhov, W J Goedheer, C J Lee, V V Ivanov, V M Krivtsum, K N Koshelev, D V Lopaev, F Bijkerk, and

V Y Banine. Exploring the electron density in plasma induced by EUV radiation : I . Experimental study in hydrogen.

[17] J Beckers, T H M Van De Ven, C A De Meijere, R M Van Der Horst, Van Kampen, and V Y Banine. Energy distribution functions for ions from pulsed EUV-induced plasmas in low pressure N 2 -diluted H 2 gas. pages 1–9.

[18] Osaka University Institute of Laser Engineering. GEKKO XII. `https://www.ile.osaka-u.ac.jp/eng/facilities/gxii/index.html` Accessed April 4, 2019.

[19] Osaka University Institute of Laser Engineering. LFEX. `https://www.ile.osaka-u.ac.jp/eng/facilities/lfex/index.html`,Accessed April 4, 2019.

[20] Eugene P Bertin. *Principles and practice of X-ray spectrometric analysis*. Springer Science & Business Media, 2012.

[21] Douglas A Skoog, F James Holler, and Stanley R Crouch. *Principles of instrumental analysis*. Cengage learning, 2017.

[22] *NIST Digital Library of Mathematical Functions*. F. W. J. Olver, A. B. Olde Daalhuis, D. W. Lozier, B. I. Schneider, R. F. Boisvert, C. W. Clark, B. R. Miller, B. V. Saunders, H. S. Cohl, and M. A. McClain, eds.

[23] Nozomi Tanaka, Nao Wada, Yasuyuki Kageyama, and Hiroaki Nishimura. Mitigation of debris from a laser plasma euv source and from focusing optics for thin film deposition by intense euv radiation. *High Energy Density Physics*, page 100865, 2020.

[24] Princeton Instruments. SP-2500i. `http://ridl.cfd.rit.edu/products/manuals/Acton/new/SP-2500i.pdf`,Accessed January 4, 2007.

[25] Princeton Instruments. PI-MAX4 1024f. `https://www.princetoninstruments.com/wp-content/uploads/2020/04/PIMAX4_1024f_datasheet.pdf`, Accessed March 17, 2020.

[26] Princeton Instruments. Light Field. https://www.princetoninstruments.com/wp-content/uploads/2020/04/LightField-Users-Manual-Issue-4.5-4411-0125.pdf, Accessed March 17, 2020.

[27] Masashi Shimomura. Laser plasma EUV light source debris control. Master's thesis, Graduate School of Engineering, Osaka University, Japan, 2008.

[28] W Schwanda, K Eidmann, and MC Richardson. Characterization of a flat-field grazing-incidence xuv spectrometer. *Journal of X-ray science and technology*, 4(1):8–17, 1993.

[29] R Paul Drake. *High-energy-density physics: foundation of inertial fusion and experimental astrophysics*. Springer, 2018.

[30] Bruce A. Remington. High energy density laboratory astrophysics. *Plasma Physics and Controlled Fusion*, 47(5 A), 2005.

[31] Eugene G Gamaly. The physics of ultra-short laser interaction with solids at non-relativistic intensities. *Physics Reports*, 508(4-5):91–243, 2011.

[32] H Daido, F Miki, K Mima, M Fujita, K Sawai, H Fujita, Y Kitagawa, S Nakai, and C Yamanaka. Generation of a strong magnetic field by an intense co 2 laser pulse. *Physical review letters*, 56(8):846, 1986.

[33] Ph Korneev, E d'Humières, and V Tikhonchuk. Gigagauss-scale quasistatic magnetic field generation in a snail-shaped target. *Physical Review E*, 91(4):043107, 2015.

[34] King Fai Farley Law, Yuki Abe, Philipp Korneev, Joao Santos, and Shinsuke Fujioka. Laser-driven magnetic reconnection and particle acceleration by snail-shaped target irradiation. *APS*, 2018:YP11–031, 2018.

[35] Francis F Chen. *Introduction to plasma physics*. Springer Science & Business Media, 2012.

[36] Francis F Chen et al. *Introduction to plasma physics and controlled fusion*, volume 1. Springer, 1984.

[37] José A Bittencourt. *Fundamentals of plasma physics*. Springer Science & Business Media, 2013.

[38] Dirk Wünderlich, S Dietrich, and Ursel Fantz. Application of a collisional radiative model to atomic hydrogen for diagnostic purposes. *Journal of Quantitative Spectroscopy and Radiative Transfer*, 110(1-2):62–71, 2009.

[39] Gabriele Cristoforetti, Alessandro De Giacomo, M Dell'Aglio, Stefano Legnaioli, Elisabetta Tognoni, Vincenzo Palleschi, and Nicolo Omenetto. Local thermodynamic equilibrium in laser-induced breakdown spectroscopy: beyond the mcwhirter criterion. *Spectrochimica Acta Part B: Atomic Spectroscopy*, 65(1):86–95, 2010.

[40] Da-Zhi Jin, Zhong-Hai Yang, Ping-Ying Tang, Kun-xiang Xiao, and Jing-yi Dai. Hydrogen plasma diagnosis in penning ion source by optical emission spectroscopy. *Vacuum*, 83(2):451–453, 2008.

[41] RWP McWhirter, RH Huddlestone, and SL Leonard. Spectral intensities in plasma diagnostic techniques. *eq*, 10:206, 1965.

[42] T Fujimoto, S Miyachi, and K Sawada. New density diagnostic method based on emission line intensity ratio of neutral hydrogen in an ionizing phase plasma. *Nuclear fusion*, 28(7):1255, 1988.

[43] N Konjević, M Ivković, and N Sakan. Hydrogen balmer lines for low electron number density plasma diagnostics. *Spectrochimica Acta Part B: Atomic Spectroscopy*, 76:16–26, 2012.

[44] Shivani Bhandari, Elaine M Sadler, J Xavier Prochaska, Sunil Simha, Stuart D Ryder, Lachlan Marnoch, Keith W Bannister, Jean-Pierre Macquart, Chris

Flynn, Ryan M Shannon, et al. The host galaxies and progenitors of fast radio bursts localized with the australian square kilometre array pathfinder. *The Astrophysical Journal Letters*, 895(2):L37, 2020.

[45] PMS Blackett. Xi. the magnetic field of massive rotating bodies. *The London, Edinburgh, and Dublin Philosophical Magazine and Journal of Science*, 40(301):125–150, 1949.

[46] Andreas Reisenegger. Origin and evolution of neutron star magnetic fields. *arXiv preprint astro-ph/0307133*, 2003.

[47] Gary D. Schmidt, Hugh C. Harris, James Liebert, Daniel J. Eisenstein, Scott F. Anderson, J. Brinkmann, Patrick B. Hall, Michael Harvanek, Suzanne Hawley, S. J. Kleinman, Gillian R. Knapp, Jurek Krzesinski, Don Q. Lamb, Dan Long, Jeffrey A. Munn, Eric H. Neilsen, Peter R. Newman, Atsuko Nitta, David J. Schlegel, Donald P. Schneider, Nicole M. Silvestri, J. Allyn Smith, Stephanie A. Snedden, Paula Szkody, and Dan Vanden Berk. Magnetic white dwarfs from the sloan digital sky survey: the first data release. *The Astrophysical Journal*, 595:1101–1113, 2003.

[48] Jonathan Tennyson. *Astronomical spectroscopy: an introduction to the atomic and molecular physics of astronomical spectra*, volume 2. World Scientific, 2010.

[49] J. E. Barnes, Kenneth Wood, Alex S. Hill, and L. M. Haffner. Photoionization and heating of a supernova-driven turbulent interstellar medium. *Monthly Notices of the Royal Astronomical Society*, 440(4):3027–3035, 2013.

[50] DR Farley, K Shigemori, and H Azechi. Laser-produced blast wave and numerical simulation using the flash code. *Laser and Particle Beams*, 23(4):513, 2005.

[51] Fang Qian, Pui Ching Lan, Megan C. Freyman, Wen Chen, Tianyi Kou, Tammy Y. Olson, Cheng Zhu, Marcus A. Worsley, Eric B. Duoss, Christopher M. Spadaccini, Ted Baumann, and T. Yong Jin Han. Ultralight Conductive Silver Nanowire Aerogels. *Nano Letters*, 17(12):7171–7176, 2017.

[52] S Eliezer. The interaction of high-power lasers with plasmas. *Plasma Physics and Controlled Fusion*, 45(2):181, 2003.

[53] I. I. Sobelman. *Theory of Atomic Spectra*. Alpha Science International Ltd, 2006.

[54] F. Paschen and E. Back. Normale und anomale zeemaneffekte. *Annalen der Physik*, 344(15):897–932, 1912.

[55] Paul A Tipler and Ralph Llewellyn. *Modern physics*. Macmillan, 2003.

[56] S. S. Harilal, C. V. Bindhu, Riju C. Issac, V. P. N. Nampoori, and C. P. G. Vallabhan. Electron density and temperature measurements in a laser produced carbon plasma. *Journal of Applied Physics*, 82(5):2140–2146, 1997.

[57] Hans R Griem. *Plasma spectroscopy*. New York : McGraw-Hill, 1964.

[58] H.-K. Chung, M.H. Chen, W.L. Morgan, Y. Ralchenko, and R.W. Lee. FLYCHK: Generalized population kinetics and spectral model for rapid spectroscopic analysis for all elements. *High Energy Density Physics*, 1(1):3 – 12, 2005.

[59] S. Ferri, A. Calisti, C. Mossé, L. Mouret, B. Talin, M. A. Gigosos, M. A. González, and V. Lisitsa. Frequency-fluctuation model applied to stark-zeeman spectral line shapes in plasmas. *Phys. Rev. E*, 84:026407, Aug 2011.

[60] E. Stambulchik, K. Tsigutkin, and Y. Maron. Spectroscopic method for measuring plasma magnetic fields having arbitrary distributions of direction and amplitude. *Physical Review Letters*, 98(22):1–4, 2007.

[61] S. Ferri, A. Calisti, C. Mossé, L. Mouret, B. Talin, M. A. Gigosos, M. A. González, and V. Lisitsa. Frequency-fluctuation model applied to Stark-Zeeman spectral line shapes in plasmas. *Physical Review E - Statistical, Nonlinear, and Soft Matter Physics*, 84(2):1–6, 2011.

[62] V. T. Tikhonchuk, M. Bailly-Grandvaux, J. J. Santos, and A. Poyé. Quasistationary magnetic field generation with a laser-driven capacitor-coil assembly. *Physical Review E*, 96(2):1–10, 2017.

[63] RL Hibbard and MJ Bono. An overview of the target fabrication operations at lawrence livermore national laboratory. *Proc. ASPE Spring Topl. Mtg*, pages 18–19, 2005.

[64] Apple.Inc. A14 Bionic. `https://www.apple.com/iphone-12/`, Accessed October 14, 2020.

[65] H Kossmann, O Schwarzkopf, B Kammerling, W Braun, and V Schmidt. Photoionisation cross section of h2. *Journal of Physics B: Atomic, Molecular and Optical Physics*, 22(14):L411, 1989.

[66] YM Chung, E-M Lee, T Masuoka, and James AR Samson. Dissociative photoionization of h2 from 18 to 124 ev. *The Journal of chemical physics*, 99(2):885–889, 1993.

[67] MMJW Van Herpen, DJW Klunder, WA Soer, R Moors, and V Banine. Sn etching with hydrogen radicals to clean euv optics. *Chemical Physics Letters*, 484(4-6):197–199, 2010.

[68] D Ugur, AJ Storm, R Verberk, JC Brouwer, and WG Sloof. Decomposition of snh4 molecules on metal and metal–oxide surfaces. *Applied surface science*, 288:673–676, 2014.

[69] Hans R Griem, Alan C Kolb, and KY Shen. Stark broadening of hydrogen lines in a plasma. *Physical Review*, 116(1):4, 1959.

[70] WL Wiese, DR Paquette, and JE Solarski. Profiles of stark-broadened balmer lines in a hydrogen plasma. *Physical review*, 129(3):1225, 1963.

[71] CS Lee, DM Camm, and GH Copley. Van der waals broadening of argon absorption lines. *Journal of Quantitative Spectroscopy and Radiative Transfer*, 15(3):211–216, 1975.

[72] F Sánchez-Bajo and FL Cumbrera. The use of the pseudo-voigt function in the variance method of x-ray line-broadening analysis. *Journal of Applied Crystallography*, 30(4):427–430, 1997.

[73] GK Wertheim, MA Butler, KW West, and DNE Buchanan. Determination of the gaussian and lorentzian content of experimental line shapes. *Review of Scientific Instruments*, 45(11):1369–1371, 1974.

[74] RM Van Der Horst, J Beckers, EA Osorio, and VY Banine. Exploring the electron density in plasmas induced by extreme ultraviolet radiation in argon. *Journal of Physics D: Applied Physics*, 48(28):285203, 2015.

[75] HA Lorentz. The absorption and emission lines of gaseous bodies. In *Knaw, Proceedings*, volume 8, pages 1905–1906, 1906.

[76] U Frisch and A Brissaud. Theory of stark broadeningâĂŤi soluble scalar model as a test. *Journal of Quantitative Spectroscopy and Radiative Transfer*, 11(12):1753–1766, 1971.

[77] Earl W Smith, J Cooper, and CR Vidal. Unified classical-path treatment of stark broadening in plasmas. *Physical Review*, 185(1):140, 1969.

[78] Marco A Gigosos and Valentín Cardeñoso. New plasma diagnosis tables of hydrogen stark broadening including ion dynamics. *Journal of Physics B: Atomic, Molecular and Optical Physics*, 29(20):4795, 1996.

[79] JM Palomares, S Hübner, EAD Carbone, N De Vries, EM Van Veldhuizen, A Sola, A Gamero, and JJAM Van Der Mullen. Hβ stark broadening in cold plasmas with low electron densities calibrated with thomson scattering. *Spectrochimica Acta Part B: Atomic Spectroscopy*, 73:39–47, 2012.

[80] OriginLab. OriginPro. `https://www.originlab.com`, Accessed October 19, 2018.

[81] H. Kossmann, O. Schwarzkopf, B. Kammerling, W. Braun, and V. Schmidt. Photoionisation cross section of H 2. *Journal of Physics B: Atomic, Molecular and Optical Physics*, 22(14), 1989.

[82] Takashi Fujimoto. Kinetics of ionization-recombination of a plasma and population density of excited ions. ii. ionizing plasma. *Journal of the physical society of Japan*, 47(1):273–281, 1979.

[83] Takashi Fujimoto. Kinetics of ionization-recombination of a plasma and population density of excited ions. iv. recombining plasma–low-temperature case. *Journal of the physical society of Japan*, 49(4):1569–1576, 1980.

[84] Takashi Fujimoto. Kinetics of ionization-recombination of a plasma and population density of excited ions. v. ionization-recombination and equilibrium plasma. *Journal of the physical society of Japan*, 54(8):2905–2914, 1985.

[85] Motoshi Goto and Shigeru Morita. Ionization balance in the rotating radiation belt accompanying complete divertor detachment in lhd. *Plasma and Fusion Research*, 3:S1042–S1042, 2008.

[86] Motoshi Goto, Keiji Sawada, and Takashi Fujimoto. Relations between the ionization or recombination flux and the emission radiation for hydrogen and helium in plasma. *Physics of Plasmas*, 9(10):4316–4324, 2002.

[87] W. M. Haynes. *CRC Handbook of Chemistry and Physics*. CRC Press, 97th editi edition.

Publication List

1. Chang Liu, Kazuki Matsuo, Sandrine Ferri, Hyun-Kyung Chung, Seungho Lee, Shohei Sakata, King Fai Farley Law, Hiroki Morita, Bradley Pollock, John Moody, Shinsuke Fujioka. Design of zeeman spectroscopy experiment with magnetized sili- con plasma generated in the laboratory. *High Energy Density Physics*, 33:100710, 2019.

2. Kazuki Matsuo, Sano Takayoshi, Kazuki Ishigure, Kato Hiroki, Natsuko Nagamatsu, Zhu Baojun, Guo Shuwang, Hideo Nagatomo, Nicolai Philippe, Youichi Sakawa, Yasunobu Arikawa, Shohei Sakata, Lee Seungho, King Fai Farley Law, Hiroki Morita, Liu Chang, Li Huan, Jo Nishibata, Ryunosuke Takizawa, Hiroshi Azechi, Shinsuke Fujioka. Flash X-ray backlight technique using a Fresnel phase zone plate for measuring interfacial instability. *High Energy Density Physics*, 100837, 2020.

3. Huan Li, Shohei Sakata, Tomoyuki Johzaki, Xiaobin Tang, Kazuki Matsuo, Seungho Lee, King Fai Farley Law, Yasunobu Arikawa, Yugo Ochiai, Chang Liu, Jo Nishibata, Ryunosuke Takizawa, Hiroki Morita, Hiroshi Azechi, Yasuhiko Sentoku, Shinsuke Fujioka. Enhanced relativistic electron beams intensity with self-generated resistive magnetic field. *High Energy Density Physics*, 100773, 2020